Sr-Nd-Pb-Hf isotope systematics of the Hugo Dummett Cu-Au porphyry deposit (Oyu Tolgoi, Mongolia)

A. Dolgopolova[a*], R. Seltmann[a], R. Armstrong[a], E. Belousova[b], R.J. Pankhurst[c] and I. Kavalieris[d]

[a] *NHM, Department of Earth Sciences, CERCAMS, London SW7 5BD, UK* [b]

[b]*Australian Research Council Centre of Excellence for Core to Crust Fluid Systems GEMOC, Macquarie University, NSW, 2109 Australia*

[c]*BGS, Keyworth, Nottingham NG12 5GG, UK*

[d]*Oyu Tolgoi LLC, Ulaanbaatar 14240, Mongolia*

Abstract

Major and trace element geochemistry including Sr-Nd-Pb-Hf isotopic data are presented for a representative sample suite of Late Devonian to Early Carboniferous plutonic and volcanic rocks from the Hugo Dummett deposit of the giant Oyu Tolgoi porphyry Cu-Au district in the South Gobi, Mongolia. Sr and Nd isotopes (whole-rock) show restricted ranges of initial compositions, with positive εNdt mainly between +3.4 and +7.4 and ($^{87}Sr/^{86}Sr$)t predominantly between 0.7037 and 0.7045 reflecting magma generation from a relatively uniform juvenile lithophile-element depleted source. Previously dated zircons from the plutonic rocks exhibit a sample-averaged range of εHft values of +11.6 to +14.5. Depleted-mantle model ages of 420-830 (Nd) and 320-730 Ma (zircon Hf) limit the involvement of pre-Neoproterozoic crust in the petrogenesis of the intermediate to felsic calc-alkaline magmas to, at most, a minor role. Pb isotopes (whole-rock) show a narrow range of unradiogenic initial compositions: $^{206}Pb/^{204}Pb$ 17.40-17.94, $^{207}Pb/^{204}Pb$ 15.43-15.49 and $^{208}Pb/^{204}Pb$ 37.25-37.64, in agreement with Sr-Nd-Hf isotopes indicating the dominance of a mantle component. All four isotopic systems suggest that the magmas from which the large Oyu Tolgoi porphyry system was generated originated predominantly from juvenile material within the subduction-related setting of the Gurvansaihan terrane.

Keywords: Hugo Dummett, Oyu Tolgoi, Mongolia, juvenile, Sr-Nd-Hf-Pb isotopes

* Corresponding author. Address: Natural History Museum, Department of Earth Sciences, Cromwell Road, London SW7 5BD, U.K. *E-mail*: allad@nhm.ac.uk. Tel.: +44 207 9426009. Fax: +44 207 9426012.

1. Introduction

The Hugo Dummett copper-gold deposit is a part of the giant Oyu Tolgoi porphyry district in South Gobi of Mongolia (Fig. 1). The district is situated within the Central Asian Orogenic Belt (CAOB), one of the largest orogens on Earth (Khain et al., 2003; Kröner et al., 2007). The CAOB (or the Altaid Tectonic Collage, Şengör et al., 1993) is a prime example of accretionary orogeny and represents a complex pattern of Neoproterozoic to Mesozoic orogenic belts; it consists of mobile belts and microcontinental blocks (Badarch et al., 2002; Buchan et al., 2002; Kovalenko et al., 2004; Kröner et al., 2007; Windley et al., 2007; Xiao et al., 2008, 2009). It stretches for 5000 km across Asia from the Siberian Craton and the Tarim and North China Craton.

Accretionary orogens constitute major sites of continental growth and mineralisation; they form at sites of subduction of oceanic lithosphere and consist of accretionary wedges containing material accreted from the downgoing plate and eroded from the upper plate, island arcs, ophiolites, oceanic plateaux, old continental blocks, metamorphic rocks and syn- and post-orogenic granitoids. Continental growth involves the addition of mantle-derived (juvenile) material to the crust (Jahn et al., 2000, 2004; Kröner et al., 2007; Cawood & Buchan, 2007). Arc magmatism within accretionary orogens is invoked as the major source of this material although extensive recycling of older continental crust may also be involved, for example in the Famatinian (Ordovician) arc of western South America (Pankhurst et al., 1998). Within the CAOB recent studies of detrital and xenocrystic zircon ages revealed that in some terranes the Precambrian crust has played an important role in the generation of the younger crust, through remelting and magmatism (Safonova et al., 2010; Rojas-Agramonte et al., 2011).

The Oyu Tolgoi group of deposits represent a typical porphyry system formed in an island-arc setting (Khashgerel et al., 2006). Majority of porphyry deposits are formed in association with subduction-related magmas (Richards, 2003). During the Paleozoic, southern Mongolia grew through the accretion of island arc, subduction,

related magmatic arcs and continental blocks. Geochemical constraints of the origin and evolution of Paleozoic magmatic arcs in the Oyu Tolgoi district using whole-rock Nd and Pb isotopes confirmed derivation of magma from a depleted mantle source in an intra-oceanic volcanic arc (Wainwright et al., 2011).

Whole-rock Sr, Nd, Pb and zircon Hf isotopic compositions were measured in 20 whole-rock samples from Late Devonian to Early Carboniferous intrusions and their volcanic host rocks in order to infer their geotectonic setting, evaluate mechanisms of crustal generation, define the composition of mantle sources, and to estimate the role of juvenile crust in the Oyu Tolgoi and nearby areas. New SHRIMP zircon ages, which will be reported in full elsewhere (Seltmann et al., *in prep.*), were obtained for most of the same samples to provide constraints on the timing of magmatism of the Hugo Dummett deposit and adjacent areas with respect to Cu–Au mineralisation.

2. Geological setting

The Oyu Tolgoi deposits are situated 650 km south of Mongolian capital Ulaanbaatar and were discovered in 1997 by BHP Billiton. The Oyu Tolgoi property comprises six main exploration prospects of Hugo Dummett (North and South), Central Oyu, South and Southwest Oyu, Heruga North and Heruga (Kavalieris et al., 2011). The geology of the six main Oyu Tolgoi deposits was summarized by Perello et al. (2001), Kirwin et al. (2005), Kavalieris and Wainwright (2005) and Khashgerel (2006, 2008). With measured and indicated resources currently amounting to 1,387 Mt at 1.33% Cu and 0.47 g/t Au, and inferred resource of 2,367 Mt at 0.78% Cu and 0.33 g/t Au (Kavalieris et al., 2011), it now comprises the largest group of Paleozoic porphyry deposits in the world.

The deposits occur in a mid Palaeozoic calc-alkaline island arc, consisting of metasediments and island arc basalts resting on an early Palaeozoic ophiolite complex (Fig. 2). Late Devonian porphyry Cu-Au deposits occur in a 22 km NNE-trending zone and are related to quartz monzodiorite intrusions emplaced in augite basalt lavas (Khashgerel et al., 2008). The Oyu Tolgoi Cu-Au porphyries are located in the Devonian Gurvansaihan terrane of Badarch (2002), which hosts many other South Gobi porphyry deposits.

The Oyu Tolgoi lithology consists of massive porphyritic augite basalt overlain by dacitic and andesitic ash flow tuff, green to red siltstone, conglomerate, carbonaceous shale and intercalated auto-brecciated basaltic lava and tuff. The nearest large outcropping felsic intrusion occurs about 3 km NW of the drilled area. Within the mineralised area, Late Devonian porphyritic quartz monzodiorite and granodiorite occur as dykes. Quartz monzodiorite bears hornblende, biotite and plagioclase; granodiorite has biotite, plagioclase and a distinctive brown aphanitic groundmass (Kirwin et al., 2005; Kavalieris and Wainwright, 2005).

This study focuses mainly on the Hugo Dummett deposits (Fig. 3) that in plan view extend for over 3 km from SW to NE. The geology, alteration and mineralisation are similar at Hugo Dummett North and Hugo Dummett South (Khashgerel, 2006). Both deposits are hosted mainly by quartz monzodiorite (Kavalieris et al., 2011). The high-grade (>2.5% Cu) sulphide mineralization is associated with intense quartz veining and is comprised of bornite, chalcocite and chalcopyrite, with the dominance of bornite. Pyrite, enargite, tetrahedrite-tennantite occur in subordinate amounts, mainly in the Hugo Dummett South. The advanced argillic alteration within the tuffs is accompanied by alunite, pyrophyllite, diaspore, dickite, topaz, zunyite and fluorite (Khashgerel et al., 2008). The sulphides exhibit a zonation from a bornite-dominated core to chalcopyrite and pyrite. Au (ppm) : Cu (%) ratios throughout much of the deposit are 1:10, but in strongly quartz-veined monzodiorite intrusions and adjacent host rocks encountered at Hugo Dummett North, this increases up to 1:1.

Figures 1-3.

3. Samples

Table 1 lists 20 drill core samples of Late Devonian to Early Carboniferous plutonic and volcanic rocks (stratigraphic zones D_3 to C_1) from within and around the Oyu Tolgoi Exploration Block (OTEB) chosen for this study; sample locations are shown in Figures 4 and 5. Four sub-samples were taken at different depths from two drill holes of OTD514 and OTD976. Stratigraphic column for samples collected from volcanic host rocks and intrusions is shown in Fig. 6. Appendix 1 includes a detailed mineralogical description for each of the studied samples.

Four samples were collected from outside of the OTEB (Fig. 4). These include: (1) a medium-grained granodiorite immediately to the north from the OTEB, (2) a dacite and (3) a quartz monzodiorite from Cu-Au mineralised intrusions 10kms to the NNE at the Ulan Khud prospect, and (4) a basalt from the Ulan Uul prospect located 24 km WSW from the OTEB.

Plutonic samples were chosen from the Hugo Dummett North and South, Oyu Tolgoi Central and Oyu Tolgoi SW to allow comparison between the main deposits.

Table 1.

Figure 4.

Figure 5.

Figure 6.

4. Analytical procedures

Whole rock analyses of major and trace elements were obtained at Activation Laboratories Ltd. (Actlabs), Ontario, Canada. Samples were prepared using a lithium metaborate / tetraborate fusion method. 0.25 g sample aliquot is digested with $HClO_4$-HNO_3-HCl-HF at 200°C to fuming and is then diluted with aqua regia. Each batch contained a method reagent blank, certified reference material, and 17% replicates. Samples were mixed with a flux of lithium metaborate and lithium tetraborate and fused in an induction furnace. The molten melt was immediately poured into a solution of 5% nitric acid containing an internal standard, and mixed continuously until completely dissolved (~30 minutes). The samples and method reagent blank were then analysed for major oxides and trace elements on a combination simultaneous/sequential Thermo Jarrell-Ash ENVIRO II ICP. For the ICP analysis, reagent blanks with and without the lithium borate flux were analysed, as well as the method reagent blank. Interference correction verification standards were analysed. Calibration was performed using multiple USGS and CANMET certified reference materials, including: GXR-1, GXR-2, WMG-1, NIST-694, NIST-696, NIST-1633b, DNC-1, BIR-1, KC-1A, CCU-1C, FK-N, LKSD-3, MAG-1, SY-3, W-2a, JSD-3, and CTA-AC-1. Two of the standards were used during the analysis for every group of ten samples. The sample solution was also spiked with internal standards and was further diluted and introduced into a Perkin Elmer SCIEX ELAN 6000 ICP/MS using a

proprietary sample introduction methodology. Further details of the analytical method, including detection limits for each element, may be found at: http://www.actlabs.com/page.aspx?page=522&app=226&cat1=549&tp=12&lk=no&menu=64

Sr-Nd-Pb isotopes were measured in the ALS Laboratory Group, Sweden. 0.2 g of rock powder was digested in a mixture of 2 ml of hydrofluoric acid and 3 ml of nitric acid in Savillex Teflon closed vials at 160^{o}C for 48 hours. All samples were prepared in duplicates. The digests were dried, dissolved in 3 ml of hydrochloric acid, heated in close vials at 160^{o}C for one hour, and evaporated to dryness. This procedure was repeated two times. Two separate aliquots of the 0.2 g digest were used. One aliquot was used for Sr and Pb column separation, where the residue was taken up in 70% HNO_3. The second aliquot was dissolved in 1 M HCl and used for Nd separation. Eichrom columns were used for element separation procedure. After purification, each element fraction was dried and re-dissolved in 5% HNO_3, ready for isotope analyses. The well-established element separation procedures for Sr can be found in Rodushkuin et al. (2007) and for Pb in Quétel et al. (2009). The isotopic analyses were performed using Neptune multi-collector ICP-MS (Thermo Fisher Scientific, Bremen, Germany) in high resolution mode (slit width of 16 μm). Element concentrations in measurement solutions for MC-ICP-MS were adjusted to required concentrations (200 ppb for Sr, 100 ppb for Pb and Nd) by dilution. Tl spike at 50 ppb was added to Pb measurement solutions for on-line mass-bias correction. Certified reference material of international standard NBS 981 for Pb, NBS 987 for Sr and Merck Nd were used to bracket the samples during the measurements. The error on the measured isotope ratios was estimated using the long-term reproducibility of repeated measurements over the time of investigation. Distilled Milli-Q water (Millipore Milli-Q) was used for preparation of all measurement solutions including standards, samples and procedural blanks, and solutions for the separation.

Hf isotope analyses were carried out at the Geochemical Analysis Unit of the GEMOC Key Centre in the Department of Earth and Planetary Sciences, Macquarie University, Australia. These analyses were performed on zircons grains dated previously by SHRIMP-II at VSEGEI, St Petersburg (Table 1). The analytical spots for the analyses were located to overlap the SHRIMP pits to avoid as far as possible

any discrepancy between the U-Pb age data and Hf-isotopic data due to any within-grain age zoning or variation. It should be noted that the zircon recovery from sample OTD388 was inadequate to define an age of crystallization, and that none of the basalts yielded zircon that could be related to crystallization of the volcanic rock. Ages for these samples were assumed as indicated in Table 1.

Hf-isotope analyses were carried out *in situ* with a New Wave UP 213nm laser-ablation microprobe, attached to a Nu Plasma multi-collector ICPMS. Typical ablation times were 80-120 s, resulting in pits 40-60 μm deep. The methodology and analyses of standard solutions and standard zircons are described by Griffin et al. (2000).

For this work we analysed masses 172, 175, 176, 177, 178, 179 and 180 simultaneously in Faraday cups; all analyses were carried out in static-collection mode. Data were normalized to $^{179}Hf/^{177}Hf=0.7325$, using an exponential correction for mass bias. Initial setup of the instrument is done using a 1 ppm solution of JMC475 Hf, which typically yields a total Hf beam of $10–14\times10^{-11}$ A.

Interference of ^{176}Lu on ^{176}Hf is corrected by measuring the intensity of the interference-free ^{175}Lu isotope and using $^{176}Lu/^{175}Lu=0.02669$ (DeBievre and Taylor, 1993) to calculate $^{176}Lu/^{177}Hf$. Similarly, the interference of ^{176}Yb on ^{176}Hf has been corrected by measuring the interference-free ^{172}Yb isotope and using $^{176}Yb/^{172}Yb$ to calculate $^{176}Yb/^{177}Hf$. The appropriate value of $^{176}Yb/^{172}Yb$ was determined by spiking the JMC475 Hf standard with Yb, and finding the value of $^{176}Yb/^{172}Yb$ (0.587) required to yield the value of $^{176}Hf/^{177}Hf$ obtained on the pure Hf solution (Griffin et al., 2004). The accuracy of the Yb and Lu corrections has been demonstrated by repeated analysis of standard zircons with a range in $^{176}Yb/^{177}Hf$ and $^{176}Lu/^{177}Hf$ (Griffin et al., 2004; Pearson et al., 2008).

For the calculation of εHf values, we have adopted the chondritic values of Blichert-Toft et al. (1997). To calculate model ages (TDM) based on a depleted-mantle source, we have adopted a model with a present-day $^{176}Hf/^{177}Hf$ of 0.28325 equivalent to average MORB and $^{176}Lu/^{177}Hf = 0.0384$ (Griffin et al., 2000). εHf values and model ages used in the figures were calculated using a decay constant for ^{176}Lu of 1.865×10^{-11}yr-1(Scherer et al., 2001). Single-stage TDM ages, which are calculated using the measured $^{176}Lu/^{177}Hf$ of the zircon can only give the minimum age for the source material of the magma from which the zircon crystallised. We therefore also calculated a two-stage “crustal” model age for each zircon (T_{DM}^{C}),

which assumes that its parental magma was produced from an average continental crust ($^{176}Lu/^{177}Hf = 0.015$) that originally was derived from depleted mantle. This is equivalent to the calculation of T_{DM}* from the Sm-Nd data.

5. Results

5.1. Major and trace elements

Whole-rock analytical results are listed in Table 2 and mantle-normalised multi-element plots are shown in Fig. 7. The latter show negative spikes for Ta, Nb and Ti for all rock types and positive spikes for Rb, Ba, Hf and Zr for all except the basalts, both of which are characteristic of subduction-related magmatism.

Table 2

Figure 7

5.2. Rare earth elements

Chondrite-normalised REE plots are shown in Fig. 8. All show slight-to-moderate light REE enrichment (La_N/Yb_N ranging from 2.4 to 15), with a slight relative depletion of the middle REE, possibly due to hornblende fractionation. Eu anomalies are negligible, except for the strong positive anomaly noted in one granodiorite (EGD 001) suggesting plagioclase accumulation.

Figure 8

5.3. Sr-Nd isotope systematics

Whole-rock samples were analysed for Sr and Nd isotope compositions (Table 3). Sm, Nd, Rb, and Sr concentration data from the geochemical analyses and U–Pb ages (Table 1) were used to calculate isotope compositions at the time of crystallization as a constraint on petrogenesis and as tracers for the crustal section through which each was emplaced. Sr-Nd analytical data are reported in Table 3. εNdt

values calculated as *per mil* deviations from the model compositions of a chondritic uniform reservoir (CHUR) at the estimated age, T_{DM} is the estimated age of extraction from depleted mantle according to the one-stage crustal pre-history assumed by DePaolo (1988), and T_{DM}* according to the two-stage model of DePaolo et al. (1991). The precision of parent/daughter ratios derived from the geochemical data is relatively low. This restricts the precision of calculated initial $^{87}Sr/^{86}Sr$ and $^{143}Nd/^{144}Nd$ ratios, which are reported here with fewer decimal places than usual. Nevertheless, errors of as much as ±10% in Rb/Sr would lead to an uncertainty of less than 0.001 in initial $^{87}Sr/^{86}Sr$ in the majority of the cases, and is only significantly higher for a few samples with $^{87}Rb/^{86}Sr$ ratios greater than about 3. In the case of the Nd isotope data a 10% error in Sm/Nd leads to an uncertainty of about 0.6 to 0.8 in εNdt. The conclusions and interpretations reached are independent of these uncertainties.

Initial $^{87}Sr/^{86}Sr$ ratios in whole-rock samples mostly fall in a restricted range of 0.7036 to 0.7045, with only three exceptions. A dacite from Hugo Dummett North (OTD 1218) has an elevated value of 0.7087, which could indicate contamination due to alteration of this ash-flow tuff sample. Two of the quartz monzodiorites from OTD514 with high Rb/Sr ratios have calculated initial $^{87}Sr/^{86}Sr$ ratios below 0.703, one of which is unrealistically low; these have been discounted in view of probably erroneous over-correction as explained above. Most of the other quartz monzodiorite samples have $^{87}Rb/^{86}Sr$ ratios <0.5, with corresponding uncertainties in their initial $^{87}Sr/^{86}Sr$ ratios of less than 0.0003. εNdt values vary from +1.5 to +7.4, with 19 of the 20 falling in the even more restricted range of +3.4 to +7.4. The dacite with the high $(^{87}Sr/^{86}Sr)t$ has an εNdt value of +4.5, strongly indicating that the Rb-Sr system was disturbed but that the Sm-Nd data is more meaningful. Regardless of the uncertainty of 0.6–0.8, it is safe to conclude that all εNdt values were significantly positive at the time of crystallization. Co-variation between the Sr and Nd isotope parameters is shown in Fig. 9, differentiated according to the rock types. Positive εNdt and low $^{87}Sr/^{86}Sr$ indicate a major contribution from long-term lithophile element depleted sources such as the mantle or juvenile crustal rocks with only a short residence time before magma genesis. These characteristics are in accordance with generation of these samples in an island arc setting of the Gurvansaihan terrane.

The late Palaeozoic depleted mantle would have had εNd values about +7 (as opposed to about +9 today), so that the slightly lower εNdt of many of the samples would permit a minor crustal contribution as well, either in the source or through contamination during magma ascent and crystallization. Normal crustal contents of Sm and Nd are higher than in basaltic magmas so that the present day isotopic compositions will largely be dominated by the crustal contribution. The approximate age of such crust may be estimated from the Nd model ages (T_{DM} and T_{DM}* in Table 3, which typically have uncertainties of 50–100 Ma due to limitations in the analytical data and model parameters).

Table 3

Figure 9

5.4. Hf isotope systematics

The results of the Lu-Hf isotope analyses of U–Pb dated zircon grains are given in Table 4. Only results for zircons clearly related to the crystallization of the parent rocks, both plutonic and dacitic, are reported, as indicated in Table 1. All 102 analyses (discounting two for grains that gave anomalous U–Pb ages) yield εHft values that are strongly positive (+10.3 to +16.1); averaged values for each sample range from +11.6 (OTD258(82.5)) to +14.5 (OTD514(1405.85-1410.15)). Considering that the standard deviation for sample mean is around one epsilon unit, the results are essentially uniform at the 2-sigma level.

Table 4

5.5. Pb isotope systematics

Table 5 shows the results of the Pb isotope analyses. The studied whole-rock samples exhibit a present-day range of $^{206}Pb/^{204}Pb$ 17.773-19.058, $^{207}Pb/^{204}Pb$ 15.445-15.544 and $^{208}Pb/^{204}Pb$ 37.456-38.489. Initial compositions were calculated using U/Pb and Th/Pb ratios taken from the geochemical data in Table 2, with a probable precision limit of about 10%, which for these sample leads to uncertainties in the

initial $^{206}Pb/^{204}Pb$ and $^{207}Pb/^{204}Pb$ ratios of, on average, ±0.05. As in the case of the initial Sr and Nd isotopic compositions in Table 3, the justification of the calculations, as well as the assumption of essentially closed system behaviour, is demonstrated by the relative uniformity of the results: in the present case the initial $^{206}Pb/^{204}Pb$, $^{207}Pb/^{204}Pb$ and $^{208}Pb/^{204}Pb$ ratios fall within the reasonably narrow ranges of 17.40-17.94, 15.43-15.49 and 37.25-37.64 respectively. Moreover, discounting the four samples for which the age corrections are highest, initial $^{206}Pb/^{204}Pb$ for the felsic rocks has an even narrower range of 17.64-17.88, and for the basalts an indistinguishable range of 17.67-17.94.

Table 5

6. Discussion and conclusions

6.1 Effects of alteration

The state of alteration of many of the samples analysed in this study (see Appendix 1 and loss-on ignition figures in Table 2) was unavoidable due to its pervasive nature within the drill cores, but an important question arises as to how this may be reflected in the results. Large-ion lithophile (LIL) elements are notoriously liable to redistribution during hydrothermal alterations; this is especially true of K and Rb, but also to a lesser extent of Sr and LREE. We do not think that such mobility has significantly affected the data and the conclusions reached for the following reasons. First, apart from a few cases identified above, the Sr and Nd isotope compositions calculated for the time of igneous emplacement are quite consistent array (initial $^{87}Sr/^{86}Sr$ 0.7038–0.7045 for both felsic and basaltic rocks; εNdt mostly +3.2 to +7.2). As noted above, there is some inverse co-variation, but all the data fall comfortably within the "mantle array" in the depleted-source field of the $^{87}Sr/^{86}Srt$ plot (Fig. 9); this could reflect either variations in the source region, or relatively minor degrees of contamination of the most LIL-depleted examples. There is no evidence for massive contamination with crustal radiogenic Sr, for example. Moreover, Khashgerel et al. (2008) show empirically that the argillic alteration at the Hugo Dummett deposit tends to reduce both K/Sr (and hence Rb/Sr) and Sm/Nd ratios, which would result in

apparently too high calculated initial $^{87}Sr/^{86}Sr$ (noticeably so for the most Rb-rich samples) as well as too high εNdt. There is clearly no evidence for such normally-co-variant behaviour. The strongest argument however is that the Sr and Nd isotope data yield conclusions as to a LIL-depleted source that are fully consistent with the evidence of Hf isotopes in zircon (average sample εHf_t +11.6 to +14.5); igneous zircon is highly resistant to chemical alteration and should preserve magmatic compositions. This is our main conclusion, but even if it were admitted that the Sr, Nd and Pb isotope systems were the product of complete equilibration with hydrothermal solutions, these would necessarily have also originated within the same magmatic system, and the alteration must have occurred very soon after igneous crystallization for all four isotope systems to record and maintain the same signature.

6.2 Indications of juvenile magmatism

In Fig. 10, εNdt is plotted against the emplacement age of each sample and model trend lines show the variation in time for depleted mantle (DM) and for 'average crust' extracted from the mantle at 1000 and 540 Ma (corresponding to the lower chronological boundaries of Neoproterozoic and Phanerozoic time). The granodiorite, monzodiorite and dacite samples plot largely within the predicted composition of early Phanerozoic crust: their model ages are little older than their mostly Late Devonian emplacement ages (420-830 Ma), confirming genesis within a relatively immature island arc system. Since the Nd model ages for the basalts are not considered meaningful, direct derivation of the felsic magmas from crust older than late Neoproterozoic can be ruled out, although a small contribution from such old material could have been mixed with dominantly juvenile magmas in the arc system.

Figure 10

Fig. 11a shows the relationship between U-Pb ages and the initial Hf isotope compositions of the individual zircon grains. All the data plot close to the estimated composition of the mid Palaeozoic depleted mantle and indicate that the parental magmas were predominantly derived from such a source, with little or no older continental crust being involved in magma genesis. This is reinforced by the T_{DM}^{C}

ages (Table 3), which range from 320 to 720 Ma, with a strong maximum close to 500 Ma (Fig. 11b). This suggests that most of these felsic igneous rocks were derived by reworking of the Early Paleozoic or younger juvenile crust that grew by the addition of magmas derived from depleted mantle.

Figures 11 a, b

Pb isotopes also indicate a source with mantle-like U-Pb ratios, relatively uncontaminated by more radiogenic Pb (Fig. 12 a, b). The basalts and dacites plot closest to the estimated composition of the Devonian MORB source, whereas the plutonic igneous rocks have slightly less radiogenic Pb, consistent with a small crustal component.

Figures 12 a, b

Nd-Hf isotope mapping of South Gobi in the frame of the CERCAMS Altaids project is shown on Fig. 13. Some published data (square symbols) are also plotted. The map shows Nd and Hf isotope signatures of granitoid samples collected by the Altaids team from hosting and surrounding terranes of the Oyu Tolgoi porphyry district. All Oyu Tolgoi samples of this study are also plotted on the map, allowing comparison of their Nd-Hf isotope signatures with other samples from the region. It is clear that the majority of samples within the South Gobi area (i.e. to the north from the North China Craton), including the Oyu Tolgoi samples of this study, exhibit dominant juvenile signatures, indicating their origin within the extensive intra-oceanic volcanic environment.

The positive initial Hf isotope values reported from the OTEB in conjunction with low apparent degrees of crustal contamination are paralleled in data reported from other significant porphyry-style deposits world wide, e.g., El Teniente, Chile (total average εHf 7.4±1.2, Muñoz et al, 2012), Mount Leyshon Igneous Complex, Australia (range of median εHf 3.2 to 4.5, Murgulov et al, 2008), Gangdese porphyry copper belt, Southern Tibet belt (εHf 1.8 to 9.2, Li et al, 2011), and Yulong porphyry system (εHf 4.6 to 6.9, Hou et al, 2011). This suggests that juvenile sources, regardless of tectonic setting play a significant role in the generation of fertile magmas required for porphyry-Cu style mineralization. As illustrated by Peytcheva et

al. (2009) and van Dongen et al. (2010), a juvenile εHf zircon signature alone is not always a sufficient indicator of magma fertility and should be assessed in conjunction with other regional petrological and structural data.

Figure 13

Acknowledgements

Ivanhoe Mines Mongolia is thanked for its continuous support and for providing samples for this study. Douglas Kirwin is especially thanked for support and inspiration. Assistance of D. Konopelko, S. Sergeev and S. Petrov with SHRIMP U-Pb zircon geochronology is highly acknowledged. This is contribution XXX from the ARC Centre of Excellence for Core to Crust Fluid Systems (http://www.ccfs.mq.edu.au) and YYY in the GEMOC Key Centre (http://www.gemoc.mq.edu.au). The Hf analytical data were obtained using instrumentation funded by DEST Systemic Infrastructure Grants, ARC LIEF, NCRIS, industry partners and Macquarie University. This is a contribution to IGCP-592 sponsored by UNESCO-IUGS.

References

Badarch, G., Cunningham, W.D. & Windley, B.F., 2002. A new terrane subdivision for Mongolia: implications for the Phanerozoic crustal growth of Central Asia. Journal of Asian Earth Sciences 21, 87–110.

Buchan, C., Pfänder, J., Kröner, A., Brewer, T., Tomurtogoo, O., Tomurhuu, D., Cunningham, D. & Windley, B. 2002. Timing of accretion and collisional deformation in the Central Asian Orogenic Belt: implications of granite geochronology in the Bayankhongor ophiolite zone. Chemical Geology, 192, 23–45.

Blichert-Toft, J.,Chauvel, C. & Albarède F. 1997. Separation of Hf and Lu for high-precision isotope analysis of rock samples by magnetic sector-multiple collector ICP-MS. Contribution to Mineralogy and Petrology, 127, 248-260.

Cawood, P.A. & Buchan C. 2007. Linking accretionary orogenesis with supercontinent assembly. Earth-Science Reviews, 82, 3–4, 217-256.

DeBievre P, Taylor PDP (1993) Table of the isotopic composition of the elements. Int. Journal of Mass Spectrometry and Ion Processes 123, 149.

DePaolo, D.J., 1981. Nd isotopes in the Colorado Front Range and crust-mantle evolution in the Proterozoic. Nature 291, 193-196.

DePaolo, D.J., 1988. Age dependence of the composition of continental crust as determined from Nd isotopic variations in igneous rocks. Earth and Planetary Science Letters 59, 263-271.

DePaolo, D.J., A.M. Linn & G. Schubert, 1991. The Continental crustal age distribution: methods of determining mantle separation ages from Sm-Nd isotopic data and application to the southwestern U.S. Journal of Geophysical Research 96, 2071-2088.

van Dongen, M., Weinberg, R.F., Tomkins, A.G., Armstrong, R.A.& Woodhead, J.D., 2010. Recycling of Proterozoic crust in Pleistocene juvenile magma and rapid formation of the Ok Tedi porphyry Cu–Au deposit, Papua New Guinea. Lithos 114, 282-292.

Griffin W. L., Pearson N. J., Belousova E. A., Jackson S. R., van Achterbergh E., O'Reilly S. Y. & Shee S. R., 2000. The Hf isotope composition of cratonic mantle: LAM-MC-ICPMS analysis of zircon megacrysts in kimberlites. Geochimica et Cosmochimica Acta 64, 133-147.

Griffin W.L., Belousova E.A., Shee S.R., Pearson N.J., O'Reilly S.Y. (2004) Archean crustal evolution in the northern Yilgam Craton: U-Pb and Hf-isotope evidence from detrital zircons. Precambrian Research 131, 231-282.

Helo, C., Hegner, E., Kroener, A., Badarch, G., Tomurtogoo, O., Windley, B.F., Dulski, P., 2006. Geochemical signature of Paleozoic accretionary complexes of the Central Asian Orogenic Belt in South Mongolia: constraints on arc environments and crustal growth. Chemical Geology 227, 236–257.

Hou, Z., Zhang, H., Pan, X. & Yang, Z. 2011. Porphyry Cu (–Mo–Au) deposits related to melting of thickened mafic lower crust: Examples from the eastern Tethyan metallogenic domain. Ore Geology Reviews 39, 21-45.

Jahn, B.M., Wu, F. & Chen, B., 2000. Massive granitoid generation in Central Asia: Nd isotope evidence and implication for continental growth in the Phanerozoic. Episodes 23, 82–92.

Jahn, B.M., Capdevila, R., Liu, D.Y., Vernon, A. & Badarch, G., 2004. Sources of Phanerozoic granitoids in the transect Bayanhongor–Ulaan Baatar, Mongolia: Geochemical and Nd isotopic evidence, and implications for Phanerozoic crustal growth: Journal of Asian Earth Sciences, 23, 629–653.

Kavalieris, I., 2005. Notes on 21 samples for zircon U-Pb geochronology from the Oyu Tolgoi Project, South Gobi Desert, Mongolia. Report Ivanhoe Mines Mongolia, 48 pp.

Kavalieris, I., Rinchin, O., Gombojav, J., Gombosuren, N., Crane, D., Orssich, C. & Khashgerel, B.-E., 2011. Characteristics of the Oyu Tolgoi porphyry deposits, South Gobi, Mongolia. Abstract volume, 11th SGA Biennial Meeting, Antofagasta, Chile, September 26 – 29, 2011, A111.

Kavalieris, I. & Wainwright, A., 2005. Wholerock geochemistry of Late Devonian island arc intrusive suites from Oyu Tolgoi. IOGD Guidebook Series, 11:169–174.

Khain, E.V., Bibikova, E.V., Salnikova, E.B., Kröner, A., Gibsher, A.S., Didenko, A.N., Degtyarev, K.E. & Fedotova, A.A., 2003. The Palaeo-Asian ocean in the Neoproterozoic and early Paleozoic: New geochronologic data and palaeotectonic reconstructions: Precambrian Research 122, 329–358.

Khashgerel, B.-E., Rye, R.O., Hedenquist, J.W. & Kavalieris, I., 2006. Geology and reconnaissance stable isotope study of the Oyu Tolgoi porphyry Cu–Au system, South Gobi, Mongolia. Economic Geology 101, 503–522.

519 Khashgerel, B.-E., Kavalieris, I. & Hayashi, K., 2008. Mineralogy, textures, and
520 whole-rock geochemistry of advanced argillic alteration: Hugo Dummett porphyry
521 Cu–Au deposit, Oyu Tolgoi mineral district, Mongolia. Mineralium Deposita 43,
522 913–932.
523 Kirwin, D. J., Forster, C.N., Kavalieris, I., Crane, D., Orssich, C., Panther, C.,
524 Garamjav, D., Munkhbat, T.O. & Niislelkhuu, G., 2005. The Oyu Tolgoi Copper-
525 Gold Porphyry Deposits, South Gobi, Mongolia: *in* Seltmann R, Gerel O and
526 Kirwin D J, (Eds.), 2005 Geodynamics and Metallogeny of Mongolia with a
527 Special Emphasis on Copper and Gold Deposits: *SEG-IAGOD Field Trip, 14-16*
528 *August 2005, 8th Biennial SGA Meeting; CERCAMS/NHM, London,* IAGOD
529 Guidebook Series 11, 155-168.
530 Kovalenko, V.I., Yarmolyuk, V.V., Kovach, V.P., Kotov, A.B., Kozakov, I.K.,
531 Salnikova, E.B. & Larin, A.M., 2004. Isotope provinces, mechanism of generation
532 and sources of the continental crust in the Central Asian mobile belt: Geological
533 and isotopic evidence: Journal of Asian Earth Sciences 23, 605–627.
534 Kröner, A., Windley, B.F., Badarch, G., Tomurtogoo, O., Hegner, E., Jahn, B.B.,
535 Grushka, S., Khain, E.V., Demoux, A. & Wingate, M.T.D., 2007. Accretionary
536 growth and crust-formation in the Central Asian Orogenic Belt and comparison
537 with the Arabian–Nubian shield. Geological Society of America, Memoirs 200:
538 181-209.
539 Li, J.-X., Qin, K.-Zh., Li, G.-M., Xiao, B., Chen, L. & Zhao, J.-X., 2011. Post-
540 collisional ore-bearing adakitic porphyries from Gangdese porphyry copper belt,
541 southern Tibet: Melting of thickened juvenile arc lower crust. Lithos 126, 265-277.
542 McDonough, W.F. & Sun, S.S., 1995. The composition of the Earth. Chemical
543 Geology 120 (3–4), 223–253.
544 Muñoz, M., Charrier, R., Fanning, C.M., Maksaev, V. & Deckart, K., 2012. Zircon
545 trace element and O-Hf isotope analyses of mineralized intrusions from El
546 Teniente ore deposit, Chilean Andes: constraints on the source and magmatic
547 evolution of porphyry Cu-Mo related magmas. Journal of Petrology 53 (6), 1091-
548 1122.
549 Murgulov, V., O'Reilly, S.Y., Griffin, W.L. & Blevin, Ph.L., 2008. Magma sources
550 and gold mineralisation in the Mount Leyshon and Tuckers Igneous Complexes,
551 Queensland, Australia: U-Pb and Hf isotope evidence. Lithos 101, 281–307.

552 Pankhurst, R.J., Rapela, C.W., Saavedra, J., Baldo, E., Dahlquist, J., Pascua, I. &
553 Fanning, C.M., 1998. The Famatinian magmatic arc in the southern Sierras
554 Pampeanas. In Pankhurst, R.J. & Rapela, C.W. (eds). The Proto-Andean Margin
555 of Gondwana. Special Publication of the Geological Society, London 142, 343-
556 367.
557 Pearson, N.J., Griffin, W.L. & O'Reilly S.Y., 2008. Mass fractionation correction in
558 laser ablation-multiple collector ICP-MS: implications for overlap corrections and
559 precise and accurate in situ isotope ratio measurement. *In P. Sylvester (Ed.),*
560 Laser-Ablation-ICP-MS in the Earth Sciences: Current Practices and Outstanding
561 Issues. Mineralogical Association of Canada Short Course 40 Vancouver, B.C., pp.
562 93-116.
563 Perello, J., Cox, D., Garamjav, D., Sanjdorj, S., Diakov, S., Schissel, D., Munkhbat,
564 T.-O. & Oyun, G., 2001. Oyu Tolgoi, Mongolia; Siluro-Devonian porphyry Cu–
565 Au–(Mo) and high-sulfidation Cu mineralization with a Cretaceous chalcocite
566 blanket. Economic Geology 96, 1407–1428.
567 Peytcheva, I., von Quadt., A., Neubauer, F., Frank, M., Nedialkov., R., Heinrich, C. &
568 Strashimirov, S. 2009. U–Pb dating, Hf-isotope characteristics and trace-REE-
569 patterns of zircons from Medet porphyry copper deposit, Bulgaria: implications
570 for timing, duration and sources of ore-bearing magmatism. Mineralogy and
571 Petrology 96, 19-41.
572 Quétel, C.R., Ponzevera, E., Rodushkin, I., Gerdes, A., Williams, A. & Woodhead, J.,
573 2009. Measuring 0.01‰ to 0.1‰ isotopic variations by MC-ICPMS –testing
574 limits for the first time with Pb δ-iCRMs. Journal of Analytical Atomic
575 Spectrometry, 24, 407-412.
576 Richards, J.P., 2003. Tectono-magmatic precursors for geophysical data over a copper
577 gold porphyry Cu-(Mo-Au) deposit formation: Economic Geology 98, 1515–1533.
578 Rodushkin, I., Bergman, T., Douglas, G., Engström, E., Sörlin, D. & Baxter, D.C.,
579 2007. Authentication of Kalix (N.E. Sweden) vendace caviar using inductively
580 coupled plasma-based analytical techniques: Evaluation of different approaches.
581 Analytica Chimica Acta 583, 310–318.
582 Rojas-Agramonte, Y., Kröner, A., Demoux, A., Xia, X., Wang, W., Donskaya, T., Liu,
583 D. & Sun, M., 2011. Detrital and xenocrystic zircon ages from Neoproterozoic to
584 Palaeozoic arc terranes of Mongolia: Significance for the origin of crustal
585 fragments in the Central Asian Orogenic Belt. Gondwana Research 19: 751-763.

586 Safonova, I., Maruyama, S., Hirata, T., Kon, Y. & Shuji Rino, S., 2010. LA ICP MS
587 U–Pb ages of detrital zircons from Russia largest rivers: Implications for major
588 granitoid events in Eurasia and global episodes of supercontinent formation.
589 Journal of Geodynamics 50, 134–153.
590 Seltmann, R. & Porter, T.M., 2005. The porphyry Cu–Au/Mo deposits of Central
591 Eurasia: 1. Tectonic, geologic and metallogenic setting and significant deposits.
592 In: Porter, T.M. (Ed.), Super Porphyry Copper and Gold Deposits: A Global
593 Perspective, vol. 2. PGC Publishing, Adelaide, 467–512.
594 Seltmann et al. Bipolar ages from zonal ongrowth of zircon at the Hugo Dummett Cu-
595 Au porphyry deposit (Oyu Tolgoi, Mongolia), Ore Geology Reviews, *in prep*.
596 Şengör, A.M.C., Natal'in, B.A., Burtman, V.S., 1993. Evolution of the Altaid tectonic
597 collage and Paleozoic crustal growth in Eurasia: Nature 364, 299–307.
598 Scherer E., Munker C. & Mezger K., 2001. Calibration of the Lutetium-Hafnium
599 clock. Science 293, 683-687.
600 Stacey, J.S. & Kramers, J.D., 1975. Approximation of terrestrial lead isotope
601 evolution by a two stage model. Earth and Planetary Science Letters 26 207–221.
602 Sun, S.S., McDonough, W.F., 1989. Chemical and isotopic systematics of oceanic
603 basalts: implications for mantel composition and processes. In: Saunders, A.D.,
604 Norry, M.J. (Eds.), Magmatism in ocean basins: Geological Society of London,
605 Special Publication, 42, pp. 313–342.
606 Taylor, S.R. & McLennan, S.M., 1985. The Continental Crust: its Composition and
607 Evolution. Blackwell Scientific Publications.
608 Wainwright, A. J., Tosdal, R. M., Wooden, J.L., Mazdab, F.K. & Friedman, R.M.,
609 2011. U–Pb (zircon) and geochemical constraints on the age, origin, and evolution
610 of Paleozoic arc magmas in the Oyu Tolgoi porphyry Cu–Au district, southern
611 Mongolia, Gondwana Research 19, 764–787.
612 Windley, B.F., Alexeiev, D., Xiao, W., Kröner, A. & Badarch, G., 2007. Tectonic
613 models for accretion of the Central Asian Orogenic Belt. Journal of the Geological
614 Society 164, 31–47.
615 Xiao, W.J., Pirajno, F. & Seltmann, R., 2008. Geodynamics and metallogeny of the
616 Altaid orogen. Journal of Asian Earth Sciences 32, 77-81.
617 Xiao, W., Windley, B.F., Huang, B.C., Han, C.M., Yuan, C., Chen, H.L., Sun, M.,
618 Sun, S. & Li, J.L., 2009. End-Permian to mid-Triassic termination of the
619 accretionary processes of the southern Altaids: implications for the geodynamic

evolution, Phanerozoic continental growth, and metallogeny of Central Asia. International Journal of the Earth Sciences 98 (6), 1189–1217.

Zartman, R.E., Doe, B.R., 1981. Plumbotectonics; the model. Tectonophysics 75, 135–162.

Appendix 1

Figure Captions

Figure 1. Tectonic setting of the Oyu Tolgoi porphyry Cu-Au deposits, Mongolia. The upper diagram illustrates the location of the Oyu Tolgoi deposit and the Gurvansayhan Terrane within the tectonic framework of Mongolia. After Kirwin et al. (2005), Ivanhoe Mines (2005), Wainwright et al. (2004) and references cited therein, Perello et al. (2001) and references cited therein (after Seltmann and Porter, 2005).

Figure 2. Regional geological setting of the Oyu Tolgoi porphyry Cu-Au deposits, Mongolia. The figure represents the outcrop geology surrounding the Oyu Tolgoi group of deposits. Sources same as in Fig. 1 (from Seltmann and Porter, 2005).

Figure 3. District scale geological setting of the Oyu Tolgoi porphyry Cu-Au deposits, Mongolia. The plan shows the interpreted solid sub-crop geology in the immediate vicinity of the deposits. Sources same as in Fig. 1 (from Seltmann and Porter, 2005).

Figure 4. General sample location map, showing pluton-sized intrusions.

Figure 5. Simplified geology of the Oyu Tolgoi Exploration Block and drill hole locations of samples included in this study.

Figure 6. Stratigraphy and location of samples included in this study (after Kavalieris, 2005).

Figure 7. Mantle-normalized multi-element diagram of the bulk rock samples from the study area (primitive mantle values are taken from McDonough and Sun, 1995).

Figure 8. Chondrite-normalized REE patterns of samples from the Oyu Tolgoi exploration block and adjacent areas; chondrite values taken from Sun and McDonough (1989).

Figure 9. Co-variation between the Sr and Nd parameters. The Nd data are considered more robust and show that all samples were derived from un-evolved sources typical of primitive island arcs.

Figure 10. εNd plotted versus the emplacement age of each body.

Figures 11 a, b. Results of zircon Hf isotope measurements for felsic igneous rocks from Oyu Tolgoi. a) Initial $^{176}Hf/^{177}Hf$ plotted against U-Pb age for individual zircon grains; compared to model lines for the evolution of deplted mantle and a chondritic reservoir (CHUR); b) Relative probability plot for the two-stage crustal residence ages calculated for each analysed spot.

Figures 12 a, b. Initial $^{207}Pb/^{204}Pb$ vs. $^{206}Pb/^{204}Pb$ and $^{208}Pb/^{204}Pb$ vs. $^{206}Pb/^{204}Pb$ plots showing results for plutonic and volcanic rocks from Oyu Tolgoi and surrounding areas. LC, lower crust; CC, continental crust; UC, upper crust; OR, orogene; M, mantle (from Zartman and Doe, 1981).

Figure 13. εHf and εNd data plotted for the South Gobi area (compilation of the CERCAMS Altaids project) and samples of this study.
Note: strongly crustal: εHf <-5, εNd(t) <-7; crustal: εHf -5 to 0, εNd(t) -7 to -2; mixed: εHf 0 to +5, εNd(t) -2 to 0; juvenile: εHf +5 to +10, εNd(t) 0 to +5; strongly juvenile: εHf >+10, εNd(t) >+5.

Table and Appendix Captions

Table 1. Sample list with U-Pb zircon ages of samples from the study area (Kavalieris, 2005; Seltmann et al., in preparation).

Table 2. Whole rock geochemical data for samples from the Oyu Tolgoi exploration block and adjacent areas.

Table 3. Sm and Nd isotope data for samples from the Oyu Tolgoi exploration block and adjacent areas.

Table 4. Lu-Hf isotope analyses of U–Pb dated zircon grains.

Table 5. Pb isotope data for samples from the Oyu Tolgoi exploration block and adjacent areas.

Appendix 1. Mineralogical description of studied samples.

Sr-Nd-Pb-Hf isotope systematics of the Hugo Dummett Cu-Au porphyry deposit (Oyu Tolgoi, Mongolia)

A. Dolgopolova[a*], R. Seltmann[a], R. Armstrong[a], E. Belousova[b], R.J. Pankhurst[c], and I. Kavalieris[d] and D. Kirwin[d]

[a] *NHM, Department of Earth Sciences, CERCAMS, London SW7 5BD, UK*

[b] *Australian Research Council Centre of Excellence for Core to Crust Fluid Systems, GEMOC, Macquarie University, NSW, 2109 Australia*

[c] *BGS, Keyworth, Nottingham NG12 5GG, UK*

[d] *Oyu Tolgoi LLC, Ulaanbaatar 14240, Mongolia*

Formatted: Font: Times New Roman, 12 pt, Italic, Font color: Auto

Formatted: Font: Times New Roman, 12 pt, Italic

Abstract

Major and trace element geochemistry including Sr-Nd-Pb-Hf isotopic data are presented for a representative sample suite of Late Devonian to Early Carboniferous plutonic and volcanic rocks from the Hugo Dummett deposit of the giant Oyu Tolgoi porphyry Cu-Au district in the South Gobi, Mongolia. Sr and Nd isotopes (whole-rock) show restricted ranges of initial compositions, with positive εNdt mainly between +3.4 and +7.4 and ($^{87}Sr/^{86}Sr$)t predominantly between 0.7037 and 0.7045 reflecting magma generation formation from a relatively uniform juvenile lithophile-element depleted source. Previously dated zircons from the plutonic rocks exhibit a sample-averaged range of εHft values of +11.6 to +14.5. Depleted-mantle model ages of 420-830 (Nd) and 320-730 Ma (zircon Hf) limitpreclude the involvement of pre-Neoproterozoic crust in the petrogenesis of the intermediate to felsic calc-alkaline magmas to, at most, a minor role. Pb isotopes (whole-rock) show a narrow range of unradiogenic initial compositions: $^{206}Pb/^{204}Pb$ 17.40-17.94, $^{207}Pb/^{204}Pb$ 15.43-15.49 and $^{208}Pb/^{204}Pb$ 37.25-37.64, in agreement with Sr-Nd-Hf isotopes indicating the dominance of a mantle component. All four isotopic systems suggest that the magmas from which the large Oyu Tolgoi porphyry system was generated originated predominantly from juvenile material within the subduction-related setting of the Gurvansaihan terrane.

Keywords: Hugo Dummett, Oyu Tolgoi, Mongolia, juvenile, Sr-Nd-Hf-Pb isotopes

* Corresponding author. Address: Natural History Museum, Department of Earth Sciences~~Mineralogy~~, Cromwell Road, London SW7 5BD, U.K. *E-mail*: allad@nhm.ac.uk. Tel.: +44 207 9426009. Fax: +44 207 9426012.

1. Introduction

The Hugo Dummett copper-gold deposit is a part of the giant Oyu Tolgoi porphyry district in South Gobi of Mongolia (Fig. 1). The district is situated within the Central Asian Orogenic Belt (CAOB), one of the largest orogens on Earth (Khain et al., 2003; Kröner et al., 2007). The CAOB (or the Altaid Tectonic Collage, Şengör et al., 1993) is a prime example of accretionary orogeny and represents a complex pattern of Neoproterozoic to Mesozoic orogenic belts; it consists of mobile belts and microcontinental blocks (Badarch et al., 2002; Buchan et al., 2002; Kovalenko et al., 2004; Kröner et al., 2007; Windley et al., 2007; Xiao et al., 2008, 2009). It stretches for 5000 km across Asia from the Siberian Craton and the Tarim and North China Craton.

Accretionary orogens constitute major sites of continental growth and mineralisation; they form at sites of subduction of oceanic lithosphere and consist of accretionary wedges containing material accreted from the downgoing plate and eroded from the upper plate, island arcs, ophiolites, oceanic plateaux, old continental blocks, metamorphic rocks and syn- and post-orogenic granitoids. Continental growth involves the addition of mantle-derived (juvenile) material to the crust (Jahn et al., 2000, 2004; Kröner et al., 2007; Cawood & Buchan, 2007). Arc magmatism within accretionary orogens is invoked as the major source of this material although extensive recycling of older continental crust may also be involved, for example in the Famatinian (Ordovician) arc of western South America (Pankhurst et al., 1998). Within the CAOB recent studies of detrital and xenocrystic zircon ages revealed that in some terranes the Precambrian crust has played an important role in the generation of the younger crust, through remelting and magmatism (Safonova et al., 2010; Rojas-Agramonte et al., 2011).

The Oyu Tolgoi group of deposits represent a typical porphyry system formed in an island-arc setting (Khashgerel et al., 2006). Majority of ~~P~~porphyry deposits are formed in association with subduction-related magmas (Richards, 2003). During the Paleozoic, southern Mongolia grew through the accretion of island arc, subduction,

related magmatic arcs and continental blocks. Geochemical constraints of the origin and evolution of Paleozoic magmatic arcs in the Oyu Tolgoi district using whole-rock Nd and Pb isotopes confirmed derivation of magma from a depleted mantle source in an intra-oceanic volcanic arc (Wainwright et al., 2011).

Whole-rock Sr, Nd, Pb and zircon Hf isotopic compositions were measured in 20 whole-rock samples from Late Devonian to Early Carboniferous intrusions and their volcanic host ~~host~~ rocks ~~hosting the intrusions~~ in order to infer their geotectonic setting, evaluate mechanisms of crustal generation, define the composition of mantle sources, and to estimate the role of juvenile crust in the Oyu Tolgoi and nearby areas. New SHRIMP zircon ages, which will be reported in full elsewhere (Seltmann et al., *in prep.*), were obtained for most of the same samples to provide constraints on the timing of magmatism of the Hugo Dummett deposit and adjacent areas with respect to Cu–Au mineralisation.

2. Geological setting

The Oyu Tolgoi deposits are situated 650 km south of Mongolian capital Ulaanbaatar and were discovered in 1997 by BHP Billiton. The Oyu Tolgoi property comprises six main exploration prospects of Hugo Dummett (North and South), Central Oyu, South and Southwest Oyu, Heruga North and Heruga (Kavalieris et al., 2011). The geology of the six main Oyu Tolgoi deposits was summarized by Perello et al. (2001), Kirwin et al. (2005), Kavalieris and Wainwright (2005) and Khashgerel (2006, 2008). With measured and indicated resources currently amounting to 1,387 Mt at 1.33% Cu and 0.47 g/t Au, and inferred resource of 2,367 Mt at 0.78% Cu and 0.33 g/t Au (Kavalieris et al., 2011), it now comprises the largest group of Paleozoic porphyry deposits in the world.

The deposits occur in a mid Palaeozoic calc-alkaline island arc, consisting of metasediments and island arc basalts resting on an early Palaeozoic ophiolite complex (Fig. 2). Late Devonian porphyry Cu-Au deposits occur in a 22 km NNE-trending zone and are related to quartz monzodiorite intrusions emplaced in augite basalt lavas (Khashgerel et al., 2008). The ~~Cu-Au~~ Oyu Tolgoi Cu-Au porphyries are located in the Devonian Gurvansaihan terrane of Badarch (2002), which hosts many other South Gobi porphyry deposits.

The Oyu Tolgoi lithology consists of massive porphyritic augite basalt overlain by dacitic and andesitic ash flow tuff, green to red siltstone, conglomerate, carbonaceous shale and intercalated auto-brecciated basaltic lava and tuff. The nearest large outcropping felsic intrusion occurs about 3 km NW of the drilled area. Within the mineralised area, Late Devonian porphyritic quartz monzodiorite and granodiorite occur as dykes. Quartz monzodiorite bears hornblende, biotite and plagioclase; granodiorite has biotite, plagioclase and a distinctive brown aphanitic groundmass (Kirwin et al., 2005; Kavalieris and Wainwright, 2005).

This study focuses mainly on the Hugo Dummett deposits (Fig. 3) that in plan view extend for over 3 km from SW to NE. The geology, alteration and mineralisation are similar at Hugo Dummett North and Hugo Dummett South (Khashgerel, 2006). Both deposits are hosted mainly by quartz monzodiorite (Kavalieris et al., 2011). The high-grade (>2.5% Cu) sulphide mineralization is associated with intense quartz veining and is comprised of bornite, chalcocite and chalcopyrite, with the dominance of bornite. Pyrite, enargite, tetrahedrite-tennantite occur in subordinate amounts, mainly in the Hugo Dummett South. The advanced argillic alteration within the tuffs is accompanied by alunite, pyrophyllite, diaspore, dickite, topaz, zunyite and fluorite (Khashgerel et al., 2008). The sulphides exhibit a zonation from a bornite-dominated core to chalcopyrite and pyrite. Au (ppm) : Cu (%) ratios throughout much of the deposit are 1:10, but in strongly quartz-veined monzodiorite intrusions and adjacent host rocks encountered at Hugo Dummett North, this increases up to 1:1.

Figures 1-3.

3. Samples

Table 1 lists 20 drill core samples of Late Devonian to Early Carboniferous plutonic and volcanic rocks (stratigraphic zones D_3 to C_1) from within and around the Oyu Tolgoi Exploration Block (OTEB) chosen for this study; sample locations are shown in Figures 4 and~~,~~ 5. Four sub-samples were taken at different depths from two drill holes of OTD514 and OTD976. Stratigraphic column for samples collected from volcanic host rocks and intrusions is shown in Fig. 6. Appendix 1 includes a detailed mineralogical description for each of the studied samples.

Four samples were collected from outside of the OTEB (Fig. 4). These include: (1) a medium-grained granodiorite immediately to the north from the OTEB, (2) a dacite and (3) a quartz monzodiorite from Cu-Au mineralised intrusions 10kms to the NNE at the Ulan Khud prospect, and (4) a basalt from the Ulan Uul prospect located 24 km WSW from the OTEB.

Plutonic samples were chosen from the Hugo Dummett North and South, Oyu Tolgoi Central and Oyu Tolgoi SW to allow comparison between the main deposits.

Table 1.

Figure 4.

Figure 5.

Figure 6.

4. Analytical procedures

Whole rock analyseis of major and trace elements were obtained at Activation Laboratories Ltd. (Actlabs~~CTLABS~~) ~~laboratory~~, (Ontario, Canada. Samples were prepared using ~~) using~~ a lithium metaborate / tetraborate fusion method. ~~to digest the samples~~. 0.25 g sample aliquot is digested with $HClO_4$-HNO_3-HCl-HF at 200°C to fuming and is then diluted with aqua regia. ~~1 g of sample was digested with aqua regia and diluted to 250 ml volumetrically.~~ Each batch contained a method reagent blank, certified reference material, and 17% replicates. Samples were mixed with a flux of lithium metaborate and lithium tetraborate and fused in an induction furnace. The molten melt was immediately poured into a solution of 5% nitric acid containing an internal standard, and mixed continuously until completely dissolved (~30 minutes). The samples and method reagent blank were then analysed for major oxides and trace elements on a combination simultaneous/sequential Thermo Jarrell-Ash ENVIRO II ICP. For the ICP analysis, reagent blanks with and without the lithium borate flux were analysed, as well as the method reagent blank. Interference correction verification standards were analysed. Calibration was performed using multiple USGS and CANMET certified reference materials, including: GXR-1, GXR-2, WMG-1, NIST-694, NIST-696, NIST-1633b, DNC-1, BIR-1, KC-1A, CCU-1C, FK-N, LKSD-3, MAG-1, SY-3, W-2a, JSD-3, and CTA-AC-1. Two of the standards were used during the analysis for every group of ten samples. The sample solution was also

Formatted: Line spacing: 1.5 lines

Formatted: Font: 12 pt

Formatted: Font: 12 pt

Formatted: Font: 12 pt

spiked with internal standards and was further diluted and introduced into a Perkin Elmer SCIEX ELAN 6000 ICP/MS using a proprietary sample introduction methodology.

~~International reference materials for the metals of interest were digested at the same time. The samples and standards were analysed on a Thermo Jarrell Ash ENVIRO II simultaneous and sequential ICP, Varian Vista 735 ICP and Thermo 6500 ICP (ACTLABS Code 4B2). An in-lab standard (traceable to certified reference materials) or certified reference materials were used for quality control. More~~Further details of the analytical method~~s~~, including detection limits for each element, may be found at:

http://www.actlabs.com/page.aspx?page=522&app=226&cat1=549&tp=12&lk=no&menu=64

Formatted: Font: 12 pt

Sr-Nd-Pb isotopes were measured in the ALS Laboratory Group, Sweden. 0.2 g of rock powder was digested in a mixture of 2 ml of hydrofluoric acid and 3 ml of nitric acid in Savillex Teflon closed vials at 160^{o}C for 48 hours. All samples were prepared in duplicates. The digests were dried, dissolved in 3 ml of hydrochloric acid, heated in close vials at 160^{o}C for one hour, and evaporated to dryness. This procedure was repeated two times. Two separate aliquots of the 0.2 g digest were used. One aliquot was used for Sr and Pb column separation, where the residue was taken up in 70% HNO_3. The second aliquot was dissolved in 1 M HCl and used for Nd separation. Eichrom columns were used for element separation procedure. After purification, each element fraction was dried and re-dissolved in 5% HNO_3, ready for isotope analyses. The well-established element separation procedures for Sr can be found in Rodushkuin et al. (2007) and for Pb in Quétel et al. (2009). The isotopic analyses were performed using Neptune multi-collector ICP-MS (Thermo Fisher Scientific, Bremen, Germany) in high resolution mode (slit width of 16 µm). Element concentrations in measurement solutions for MC-ICP-MS were adjusted to required concentrations (200 ppb for Sr, 100 ppb for Pb and Nd) by dilution. Tl spike at 50 ppb was added to Pb measurement solutions for on-line mass-bias correction. Certified reference material of international standard NBS 981 for Pb, NBS 987 for Sr and Merck Nd were used to bracket the samples during the measurements. The error on the measured isotope ratios was estimated using the long-term reproducibility of repeated measurements over the time of investigation. Distilled Milli-Q water

(Millipore Milli-Q) was used for preparation of all measurement solutions including standards, samples and procedural blanks, and solutions for the separation.

~~Analytical data are reported in Table 2, together with εNdt values calculated as *per mil* deviations from the contemporaneous model compositions of a chondritic uniform reservoir (CHUR) using the determined or estimated age of each sample as in **Table 1**. Estimated ages for the extraction of the parent material were also calculated as follows: T_{DM} from depleted mantle according to the one stage crustal pre history assumed by DePaolo (1988), T_{DM}* from depleted mantle according to the two stage model of DePaolo et al. (1991).~~

Hf isotope analyses were carried out at the Geochemical Analysis Unit of the GEMOC Key Centre in the Department of Earth and Planetary Sciences, Macquarie University, Australia. These analyses were performed on zircons grains dated previously by SHRIMP-II at VSEGEI, St Petersburg (Table 1). The analytical spots for the analyses were located to overlap the SHRIMP pits to avoid as far as possible any discrepancy between the U-Pb age data and Hf-isotopic data due to any within-grain age zoning or variation. It should be noted that the zircon recovery from sample OTD388 was inadequate to define an age of crystallization, and that none of the basalts yielded zircon that could be related to crystallization of the volcanic rock. Ages for these samples were assumed as indicated in Table 1.

Hf-isotope analyses were carried out *in situ* with a New Wave UP 213nm laser-ablation microprobe, attached to a Nu Plasma multi-collector ICPMS. Typical ablation times were 80-120 s, resulting in pits 40-60 μm deep. The methodology and analyses of standard solutions and standard zircons are described by Griffin et al. (2000).

For this work we analysed masses 172, 175, 176, 177, 178, 179 and 180 simultaneously in Faraday cups; all analyses were carried out in static-collection mode. Data were normalized to $^{179}Hf/^{177}Hf=0.7325$, using an exponential correction for mass bias. Initial setup of the instrument is done using a 1 ppm solution of JMC475 Hf, which typically yields a total Hf beam of $10–14\times10^{-11}$ A.

Interference of ^{176}Lu on ^{176}Hf is corrected by measuring the intensity of the interference-free ^{175}Lu isotope and using $^{176}Lu/^{175}Lu=0.02669$ (DeBievre and Taylor, 1993) to calculate $^{176}Lu/^{177}Hf$. Similarly, the interference of ^{176}Yb on ^{176}Hf has been

Formatted: Font: Not Italic

Formatted: Font: Not Italic

corrected by measuring the interference-free ^{172}Yb isotope and using $^{176}Yb/^{172}Yb$ to calculate $^{176}Yb/^{177}Hf$. The appropriate value of $^{176}Yb/^{172}Yb$ was determined by spiking the JMC475 Hf standard with Yb, and finding the value of $^{176}Yb/^{172}Yb$ (0.587) required to yield the value of $^{176}Hf/^{177}Hf$ obtained on the pure Hf solution (Griffin et al., 2004). The accuracy of the Yb and Lu corrections has been demonstrated by repeated analysis of standard zircons with a range in $^{176}Yb/^{177}Hf$ and $^{176}Lu/^{177}Hf$ (Griffin et al., 2004; Pearson et al., 2008).

For the calculation of εHf values, we have adopted the chondritic values of Blichert-Toft et al. (1997). To calculate model ages (TDM) based on a depleted-mantle source, we have adopted a model with a present-day $^{176}Hf/^{177}Hf$ of 0.28325 equivalent to average MORB and $^{176}Lu/^{177}Hf = 0.0384$ (Griffin et al., 2000). εHf values and model ages used in the figures were calculated using a decay constant for ^{176}Lu of 1.865 x 10^{-11}yr-1(Scherer et al., 2001). Single-stage TDM ages, which are calculated using the measured $^{176}Lu/^{177}Hf$ of the zircon can only give the minimum age for the source material of the magma from which the zircon crystallised. We therefore also calculated a two-stage "crustal" model age for each zircon (T_{DM}^{C}), which assumes that its parental magma was produced from an average continental crust ($^{176}Lu/^{177}Hf = 0.015$) that originally was derived from depleted mantle. This is equivalent to the calculation~~treatment~~ of T_{DM}* from the Sm-Nd data.

5. Results

5.1. Major and trace elements

Whole-rock analytical results are listed in Table 2 and mantle-normalised multi-element plots are shown in Fig. 7. The latter show negative spikes for Ta, Nb and Ti for all rock types and positive spikes for Rb, Ba, Hf and Zr for all except the basalts, both of which are characteristic of subduction-related magmatism.

Table 2

Figure 7

5.2. Rare earth elements

Formatted: Font: Not Italic

Formatted: Font: Not Italic

Formatted: Font: Not Italic

Chondrite-normalised REE plots are shown in Fig. 8. All show slight-to-moderate light REE enrichment (La_N/Yb_N ranging from 2.4 to 15), with a slight relative depletion of the middle REE, possibly due to hornblende fractionation. Eu anomalies are negligible, except for the strong positive anomaly noted in one granodiorite (EGD 001) suggesting plagioclase accumulation.

Figure 8

5.3. Sr-Nd isotope systematics

Whole-rock samples were analysed for Sr and Nd isotope compositions (Table 3). Sm, Nd, Rb, and Sr concentration data from the geochemical analyses and U–Pb ages (Table 1) were used to calculate isotope compositions at the time of crystallization as a constraint on petrogenesis and as tracers for the crustal section through which each was emplaced. Sr-Nd analytical data are reported in Table 3. εNdt values calculated as *per mil* deviations from the model compositions of a chondritic uniform reservoir (CHUR) at the estimated age, T_{DM} is the estimated age of extraction from depleted mantle according to the one-stage crustal pre-history assumed by DePaolo (1988), and T_{DM}* according to the two-stage model of DePaolo et al. (1991). The precision of parent/daughter ratios derived from the geochemical data is relatively low. This restricts the precision of calculated initial $^{87}Sr/^{86}Sr$ and $^{143}Nd/^{144}Nd$ ratios, which are reported here with fewer decimal places than usual. Nevertheless, errors of as much as ±10% in Rb/Sr would lead to an uncertainty of less than 0.001 in initial $^{87}Sr/^{86}Sr$ in the majority of the cases, and is only significantly higher for a few samples with $^{87}Rb/^{86}Sr$ ratios greater than about 3. In the case of the Nd isotope data a 10% error in Sm/Nd leads to an uncertainty of about 0.6 to 0.8 in εNdt. The conclusions and interpretations reached are independent of these uncertainties.

~~Since the precision of the geochemical data is restricted, initial $^{87}Sr/^{86}Sr$ and $^{143}Nd/^{144}Nd$ ratios are rounded down to allow for uncertainty in the age corrections.~~

Initial $^{87}Sr/^{86}Sr$ ratios in whole-rock samples mostly fall in a restricted range of 0.7036 to 0.7045, with only three exceptions. A dacite from Hugo Dummett North (OTD 1218) has an elevated value of 0.7087, which could indicate contamination due

to alteration of this ash-flow tuff sample. Two of the quartz monzodiorites from OTD514 with high Rb/Sr ratios have calculated initial $^{87}Sr/^{86}Sr$ ratios below 0.703, one of which is unrealistically low; these have been discounted in view of probably erroneous over-correction as explained above. Most of the other quartz monzodiorite samples have $^{87}Rb/^{86}Sr$ ratios <0.5, with corresponding uncertainties in their initial $^{87}Sr/^{86}Sr$ ratios of less than 0.0003. εNdt values vary from +1.5 to +7.4, with 19 of the 20 falling in the even more restricted range of +3.4 to +7.4. The dacite with the high $(^{87}Sr/^{86}Sr)t$ has an εNdt value of +4.5, strongly indicating that the Rb-Sr system was disturbed but that the Sm-Nd data is more meaningful. Regardless of the uncertainty of 0.6–0.8, it is safe to conclude that all εNdt values were significantly positive at the time of crystallization. ~~whereas a nearby quartz monzodiorite has a low value of 0.7028 that may suggest a depleted mantle source. The value for quartz monzodiorite OTD514-1 is unrealistically low and in view of the high Rb/Sr ratio of this sample it is suggested that slight open-system behaviour has resulted in over-correction – this result is discounted. Corresponding εNdt values vary from +1.5 to +7.4, with 19 of the 20 falling in the even more restricted range of +3.4 to +7.4. The dacite with the high $(^{87}Sr/^{86}Sr)t$ has an εNdt value of +4.5, strongly indicating that the Rb-Sr system was disturbed and that the Sm-Nd data is more meaningful.~~

Co-variation between the Sr and Nd isotope parameters is shown in Fig. 9, differentiated according to the rock types. Positive εNdt and low $^{87}Sr/^{86}Sr$ indicate a major contribution from long-term lithophile element depleted sources such as the mantle or juvenile crustal rocks with only a short residence time before magma genesis. These characteristics are in accordance with generation of these samples in an island arc setting of the Gurvansaihan terrane.

The late Palaeozoic depleted mantle would have had εNd values about~~round~~ +7 (as opposed to about~~around~~ +9 today), so that the slightly lower εNdt of many of the samples would permit a minor crustal contribution as well, either in the source or through contamination during magma ascent and crystallization. Normal crustal contents of Sm and Nd are higher than in basaltic magmas so that the present day isotopic compositions will largely be dominated by the crustal contribution. The approximate age of such crust may be estimated from the Nd model ages (T_{DM} and T_{DM}* in Table 3, which typically have uncertainties of 50–100 Ma due to limitations in the analytical data and model parameters).

Table 3

Figure 9

5.4. Hf isotope systematics

The results of the Lu-Hf isotope analyses of U–Pb dated zircon grains are given in Table 4. Only results for zircons clearly related to the crystallization of the parent rocks, both plutonic and dacitic, are reported, as indicated in Table 1. All 102 analyses (discounting two for grains that gave anomalous U–Pb ages) yield εHft values that are strongly positive (+10.3 to +16.1); averaged values for each sample range from +11.6 (OTD258(82.5)) to +14.5 (OTD514(1405.85-1410.15)). Considering that the standard deviation for sample mean is around one epsilon unit, the results are essentially uniform at the 2-sigma level~~effectively indistinguishable~~.

Table 4

5.5. Pb isotope systematics

Table 5 shows the results of the Pb isotope analyses. The studied whole-rock samples exhibit a ~~narrow~~ present-day range of $^{206}Pb/^{204}Pb$ 17.773-19.058, $^{207}Pb/^{204}Pb$ 15.445-15.544 and~~&~~ $^{208}Pb/^{204}Pb$ 37.456-38.489. Initial compositions were calculated using U/Pb and Th/Pb ratios taken from the geochemical data in Table 2, with a probable precision limit of about 10%, which for these sample leads to uncertainties in the initial $^{206}Pb/^{204}Pb$ and $^{207}Pb/^{204}Pb$ ratios of, on average, ±0.05. As in the case of the initial Sr and Nd isotopic compositions in Table 3, the justification of the calculations, as well as the assumption of essentially closed system behaviour, is demonstrated by the relative uniformity of the results: in the present case the initial $^{206}Pb/^{204}Pb$, $^{207}Pb/^{204}Pb$ and $^{208}Pb/^{204}Pb$ ratios fall within the reasonably narrow ranges of 17.40-17.94, 15.43-15.49 and 37.25-37.64 respectively. Moreover, discounting the four samples for which the age corrections are highest, initial $^{206}Pb/^{204}Pb$ for the felsic rocks has an even narrower range of 17.64-17.88, and for the basalts an indistinguishable range of 17.67-17.94. ~~Calculated initial compositions assuming~~

~~closed system behavior and using the geochemical analyses for U, Th and Pb concentrations yield even narrower ranges of 17.40–17.94, 15.43–15.49 and 37.25–37.64 respectively.~~

Table 5

6. Discussion and conclusions

6.1 Effects of alteration

The state of alteration of many of the samples analysed in this study (see Appendix 1~~NEW TABLE~~ and loss-on ignition figures in Table 2) was unavoidable due to its pervasive nature within the drill cores, but an important question arises as to how this may be reflected in the results. Large-ion lithophile (LIL) elements are notoriously liable to redistribution during hydrothermal alterations; this is especially true of K and Rb, but also to a lesser extent of Sr and LREE. We do not think that such mobility has significantly affected the data and the conclusions reached for the following reasons. First, apart from a few cases identified above, the Sr and Nd isotope compositions calculated for the time of igneous emplacement are quite consistent array (initial $^{87}Sr/^{86}Sr$ 0.7038–0.7045 for both felsic and basaltic rocks; εNdt mostly +3.2 to +7.2). As noted abo~~p~~ve, there is some inverse co-variation, but all the data fall comfortably within the "mantle array" in the depleted-source field of the $^{87}Sr/^{86}Sr$t plot (Fig. 9); this could reflect either variations in the source region, or ~~a~~ relatively minor degrees of contamination of the most LIL-depleted examples. There is no evidence for massive contamination with crustal radiogenic Sr, for example. Moreover, Khashgerel et al. (2008) show empirically that the argillic alteration at the Hugo Dummett deposit tends to reduce both K/Sr (and hence Rb/Sr) and Sm/Nd ratios, which would result in apparently too high calculated initial $^{87}Sr/^{86}Sr$ (noticeably so for the most Rb-rich samples) as well as too high εNdt. There is clearly no evidence for such normally-co-variant behaviour. The strongest argument however is that the Sr and Nd isotope data yield conclusions as to a LIL-depleted source that are fully consistent with the evidence of Hf isotopes in zircon (average sample εHf_t +11.6 to +14.5); igneous zircon is highly resistant to chemical alteration and should

Formatted: Highlight

preserve magmatic compositions. This is our main conclusion, but even if it were admitted that the Sr, Nd and Pb isotope systems were the product of complete equilibration with hydrothermal solutions, these would necessarily have also originated within the same magmatic system, and the alteration must have occurred very soon after igneous crystallization for all four isotope systems to record and maintain the same signature.

6.2 Indications of ~~j~~Juvenile m~~M~~agmatism

In Fig. 10, εNdt is plotted against the emplacement age of each sample and model trend lines show the variation in time for depleted mantle (DM) and for 'average crust' extracted from the mantle at 1000 and 540 Ma (corresponding to the lower chronological boundaries of Neoproterozoic and Phanerozoic time). The granodiorite, monzodiorite and dacite samples plot largely within the predicted composition of early Phanerozoic crust: their model ages are little older than their mostly Late Devonian emplacement ages (420-830 Ma), confirming genesis within a relatively immature island arc system. Since the Nd model ages for the basalts are not considered meaningful, ~~there is no evidence of crust older than late Neoproterozoic being involved in the arc system.~~direct derivation of the felsic magmas from crust older than late Neoproterozoic can be ruled out, although a small contribution from such old material could have been mixed with dominantly juvenile magmas in the arc system.

Formatted: Indent: First line: 0 cm

Figure 10.

Fig. 11a shows the relationship between U-Pb ages and the initial Hf isotope compositions of the individual zircon grains. All the data plot close to the estimated composition of the mid Palaeozoic depleted mantle and indicate that the parental magmas were predominantly derived from such a source, with little or no older continental crust being involved in magma genesis. This is reinforced by the T_{DM}^{C} ages (Table 3), which range from 320 to 720 Ma, with a strong maximum close to 500

Ma (Fig. 11b). This suggests that most of these felsic igneous rocks were derived by reworking of the Early Paleozoic or younger juvenile crust that grew by the addition of magmas derived from depleted mantle.

Figures 11 a, b.

Pb isotopes also indicate a source with mantle-like U-Pb ratios, relatively uncontaminated by more radiogenic Pb (Fig. 12 a, b). The basalts and dacites plot closest to the estimated composition of the Devonian MORB source, whereas the plutonic igneous rocks have slightly less radiogenic Pb, consistent with a small crustal component.

Figures 12 a, b.

Nd-Hf isotope mapping of South Gobi in the frame of the CERCAMS Altaids project is shown on Fig. 13. Some published data (square symbols) are also plotted. The map shows Nd and Hf isotope signatures of granitoid samples collected by the Altaids team from hosting and surrounding terranes of the Oyu Tolgoi porphyry district. All Oyu Tolgoi samples of this study are also plotted on the map, allowing comparison of their Nd-Hf isotope signatures with other samples from the region. It is clear that the majority of samples within the South Gobi area (i.e. to the north from the North China Craton), including the Oyu Tolgoi samples of this study, exhibit dominant juvenile signatures, indicating their origin within the extensive intra-oceanic volcanic environment.

The positive initial Hf isotope values reported from the OTEB in conjunction with low apparent degrees of crustal contamination are paralleled in data reported from other significant porphyry-style deposits world wide, e.g., El Teniente, Chile (total average εHf 7.4±1.2, Muñoz et al, 2012), Mount Leyshon Igneous Complex, Australia (range of median εHf 3.2 to 4.5, Murgulov et al, 2008), Gangdese porphyry copper belt, Southern Tibet belt (εHf 1.8 to 9.2, Li et al, 2011), and Yulong porphyry system (εHf 4.6 to 6.9, Hou et al, 2011). This suggests that juvenile sources, regardless of tectonic setting play a significant role in the generation of fertile magmas required for porphyry-Cu style mineralization. As illustrated by Peytcheva et al. (2009) and van Dongen et al. (2010), a juvenile εHf zircon signature alone is not

always a sufficient indicator of magma fertility and should be assessed in conjunction with other regional petrological and structural data.

Figure 13

Acknowledgements

Ivanhoe Mines Mongolia is thanked for its continuous support and for providing samples for this study. Douglas Kirwin is especially thanked for support and inspiration. Assistance of D. Konopelko, S. Sergeev and S. Petrov with SHRIMP U-Pb zircon geochronology is highly acknowledged. ~~This is a contribution to IGCP-592 sponsored by UNESCO-IUGS.~~ This is contribution XXX from the ARC Centre of Excellence for Core to Crust Fluid Systems (http://www.ccfs.mq.edu.au) and YYY in the GEMOC Key Centre (http://www.gemoc.mq.edu.au). The Hf analytical data were obtained using instrumentation funded by DEST Systemic Infrastructure Grants, ARC LIEF, NCRIS, industry partners and Macquarie University. This is a contribution to IGCP-592 sponsored by UNESCO-IUGS.

Formatted: Normal, Line spacing: 1.5 lines

Formatted: Font: 12 pt, Not Bold, Font color: Auto

Formatted: Font: 12 pt, Font color: Auto

Formatted: Font: 12 pt, Not Bold, Font color: Auto

Formatted: Font: 12 pt, Font color: Auto

Formatted: Font: 12 pt, Not Bold, Font color: Auto

Formatted: Font: 12 pt, Font color: Auto

Formatted: Font: 12 pt

References

Badarch, G., Cunningham, W.D. & Windley, B.F., 2002. A new terrane subdivision for Mongolia: implications for the Phanerozoic crustal growth of Central Asia. Journal of Asian Earth Sciences 21, 87–110.

Buchan, C., Pfänder, J., Kröner, A., Brewer, T., Tomurtogoo, O., Tomurhuu, D., Cunningham, D. & Windley, B. 2002. Timing of accretion and collisional deformation in the Central Asian Orogenic Belt: implications of granite geochronology in the Bayankhongor ophiolite zone. Chemical Geology, 192, 23–45.

Blichert-Toft, J.,Chauvel, C. & Albarède F. 1997. Separation of Hf and Lu for high-precision isotope analysis of rock samples by magnetic sector-multiple collector ICP-MS. Contribution to Mineralogy and Petrology, 127, 248-260.

Cawood, P.A. & Buchan C. 2007. Linking accretionary orogenesis with supercontinent assembly. Earth-Science Reviews, 82, 3–4, 217-256.

DeBievre P, Taylor PDP (1993) Table of the isotopic composition of the elements. Int. Journal of Mass Spectrometry and Ion Processes 123, 149.

DePaolo, D.J., 1981. Nd isotopes in the Colorado Front Range and crust-mantle evolution in the Proterozoic. Nature 291, 193-196.

DePaolo, D.J., 1988. Age dependence of the composition of continental crust as determined from Nd isotopic variations in igneous rocks. Earth and Planetary Science Letters 59, 263-271.

DePaolo, D.J., A.M. Linn & G. Schubert, 1991. The Continental crustal age distribution: methods of determining mantle separation ages from Sm-Nd isotopic data and application to the southwestern U.S. Journal of Geophysical Research 96, 2071-2088.

van Dongen, M., Weinberg, R.F., Tomkins, A.G., Armstrong, R.A.& Woodhead, J.D., 2010. Recycling of Proterozoic crust in Pleistocene juvenile magma and rapid formation of the Ok Tedi porphyry Cu–Au deposit, Papua New Guinea. Lithos 114, 282-292.

Griffin W. L., Pearson N. J., Belousova E. A., Jackson S. R., van Achterbergh E., O'Reilly S. Y. & Shee S. R., 2000. The Hf isotope composition of cratonic mantle: LAM-MC-ICPMS analysis of zircon megacrysts in kimberlites. Geochimica et Cosmochimica Acta 64, 133-147.

520 Griffin W.L., Belousova E.A., Shee S.R., Pearson N.J., O'Reilly S.Y. (2004) Archean
521 crustal evolution in the northern Yilgam Craton: U-Pb and Hf-isotope evidence
522 from detrital zircons. Precambrian Research 131, 231-282.

523 Helo, C., Hegner, E., Kroener, A., Badarch, G., Tomurtogoo, O., Windley, B.F.,
524 Dulski, P., 2006. Geochemical signature of Paleozoic accretionary complexes of the
525 Central Asian Orogenic Belt in South Mongolia: constraints on arc environments
526 and crustal growth. Chemical Geology 227, 236–257.

527 Hou, Z., Zhang, H., Pan, X. & Yang, Z. 2011. Porphyry Cu (–Mo–Au) deposits related
528 to melting of thickened mafic lower crust: Examples from the eastern Tethyan
529 metallogenic domain. Ore Geology Reviews 39, 21-45.

530 Jahn, B.M., Wu, F. & Chen, B., 2000. Massive granitoid generation in Central Asia:
531 Nd isotope evidence and implication for continental growth in the Phanerozoic.
532 Episodes 23, 82–92.

533 Jahn, B.M., Capdevila, R., Liu, D.Y., Vernon, A. & Badarch, G., 2004. Sources of
534 Phanerozoic granitoids in the transect Bayanhongor–Ulaan Baatar, Mongolia:
535 Geochemical and Nd isotopic evidence, and implications for Phanerozoic crustal
536 growth: Journal of Asian Earth Sciences, 23, 629–653.

537 Kavalieris, I., 2005. Notes on 21 samples for zircon U-Pb geochronology from the
538 Oyu Tolgoi Project, South Gobi Desert, Mongolia. Report Ivanhoe Mines
539 Mongolia, 48 pp.

540 Kavalieris, I., Rinchin, O., Gombojav, J., Gombosuren, N., Crane, D., Orssich, C. &
541 Khashgerel, B.-E., 2011. Characteristics of the Oyu Tolgoi porphyry deposits,
542 South Gobi, Mongolia. Abstract volume, 11th SGA Biennial Meeting, Antofagasta,
543 Chile, September 26 – 29, 2011, A111.

544 Kavalieris, I. & Wainwright, A., 2005. Wholerock geochemistry of Late Devonian
545 island arc intrusive suites from Oyu Tolgoi. IOGD Guidebook Series, 11:169–174.

546 Khain, E.V., Bibikova, E.V., Salnikova, E.B., Kröner, A., Gibsher, A.S., Didenko,
547 A.N., Degtyarev, K.E. & Fedotova, A.A., 2003. The Palaeo-Asian ocean in the
548 Neoproterozoic and early Paleozoic: New geochronologic data and palaeotectonic
549 reconstructions: Precambrian Research 122, 329–358.

550 Khashgerel, B.-E., Rye, R.O., Hedenquist, J.W. & Kavalieris, I., 2006. Geology and
551 reconnaissance stable isotope study of the Oyu Tolgoi porphyry Cu–Au system,
552 South Gobi, Mongolia. Economic Geology 101, 503–522.

553 Khashgerel, B.-E., Kavalieris, I. & Hayashi, K., 2008. Mineralogy, textures, and
554 whole-rock geochemistry of advanced argillic alteration: Hugo Dummett porphyry
555 Cu–Au deposit, Oyu Tolgoi mineral district, Mongolia. Mineralium Deposita 43,
556 913–932.
557 Kirwin, D. J., Forster, C.N., Kavalieris, I., Crane, D., Orssich, C., Panther, C.,
558 Garamjav, D., Munkhbat, T.O. & Niislelkhuu, G., 2005. The Oyu Tolgoi Copper-
559 Gold Porphyry Deposits, South Gobi, Mongolia: *in* Seltmann R, Gerel O and
560 Kirwin D J, (Eds.), 2005 Geodynamics and Metallogeny of Mongolia with a
561 Special Emphasis on Copper and Gold Deposits: *SEG-IAGOD Field Trip, 14-16*
562 *August 2005, 8th Biennial SGA Meeting; CERCAMS/NHM, London,* IAGOD
563 Guidebook Series 11, 155-168.
564 Kovalenko, V.I., Yarmolyuk, V.V., Kovach, V.P., Kotov, A.B., Kozakov, I.K.,
565 Salnikova, E.B. & Larin, A.M., 2004. Isotope provinces, mechanism of generation
566 and sources of the continental crust in the Central Asian mobile belt: Geological
567 and isotopic evidence: Journal of Asian Earth Sciences 23, 605–627.
568 Kröner, A., Windley, B.F., Badarch, G., Tomurtogoo, O., Hegner, E., Jahn, B.B.,
569 Grushka, S., Khain, E.V., Demoux, A. & Wingate, M.T.D., 2007. Accretionary
570 growth and crust-formation in the Central Asian Orogenic Belt and comparison
571 with the Arabian–Nubian shield. Geological Society of America, Memoirs 200:
572 181-209.
573 Li, J.-X., Qin, K.-Zh., Li, G.-M., Xiao, B., Chen, L. & Zhao, J.-X., 2011. Post-
574 collisional ore-bearing adakitic porphyries from Gangdese porphyry copper belt,
575 southern Tibet: Melting of thickened juvenile arc lower crust. Lithos 126, 265-277.
576 McDonough, W.F. & Sun, S.S., 1995. The composition of the Earth. Chemical
577 Geology 120 (3–4), 223–253.
578 Muñoz, M., Charrier, R., Fanning, C.M., Maksaev, V. & Deckart, K., 2012. Zircon
579 trace element and O-Hf isotope analyses of mineralized intrusions from El
580 Teniente ore deposit, Chilean Andes: constraints on the source and magmatic
581 evolution of porphyry Cu-Mo related magmas. Journal of Petrology 53 (6), 1091-
582 1122.
583 Murgulov, V., O'Reilly, S.Y., Griffin, W.L. & Blevin, Ph.L., 2008. Magma sources
584 and gold mineralisation in the Mount Leyshon and Tuckers Igneous Complexes,
585 Queensland, Australia: U-Pb and Hf isotope evidence. Lithos 101, 281–307.

586 Pankhurst, R.J., Rapela, C.W., Saavedra, J., Baldo, E., Dahlquist, J., Pascua, I. &
587 Fanning, C.M., 1998. The Famatinian magmatic arc in the southern Sierras
588 Pampeanas. In Pankhurst, R.J. & Rapela, C.W. (eds). The Proto-Andean Margin
589 of Gondwana. Special Publication of the Geological Society, London 142, 343-
590 367.
591 Pearson, N.J., Griffin, W.L. & O'Reilly S.Y., 2008. Mass fractionation correction in
592 laser ablation-multiple collector ICP-MS: implications for overlap corrections and
593 precise and accurate in situ isotope ratio measurement. *In P. Sylvester (Ed.),*
594 Laser-Ablation-ICP-MS in the Earth Sciences: Current Practices and Outstanding
595 Issues. Mineralogical Association of Canada Short Course 40 Vancouver, B.C., pp.
596 93-116.
597 Perello, J., Cox, D., Garamjav, D., Sanjdorj, S., Diakov, S., Schissel, D., Munkhbat,
598 T.-O. & Oyun, G., 2001. Oyu Tolgoi, Mongolia; Siluro-Devonian porphyry Cu–
599 Au–(Mo) and high-sulfidation Cu mineralization with a Cretaceous chalcocite
600 blanket. Economic Geology 96, 1407–1428.
601 Peytcheva, I., von Quadt., A., Neubauer, F., Frank, M., Nedialkov., R., Heinrich, C. &
602 Strashimirov, S. 2009. U–Pb dating, Hf-isotope characteristics and trace-REE-
603 patterns of zircons from Medet porphyry copper deposit, Bulgaria: implications
604 for timing, duration and sources of ore-bearing magmatism. Mineralogy and
605 Petrology 96, 19-41.
606 Quétel, C.R., Ponzevera, E., Rodushkin, I., Gerdes, A., Williams, A. & Woodhead, J.,
607 2009. Measuring 0.01‰ to 0.1‰ isotopic variations by MC-ICPMS –testing
608 limits for the first time with Pb δ-iCRMs. Journal of Analytical Atomic
609 Spectrometry, 24, 407-412.
610 Richards, J.P., 2003. Tectono-magmatic precursors for geophysical data over a copper
611 gold porphyry Cu-(Mo-Au) deposit formation: Economic Geology 98, 1515–1533.
612 Rodushkin, I., Bergman, T., Douglas, G., Engström, E., Sörlin, D. & Baxter, D.C.,
613 2007. Authentication of Kalix (N.E. Sweden) vendace caviar using inductively
614 coupled plasma-based analytical techniques: Evaluation of different approaches.
615 Analytica Chimica Acta 583, 310–318.
616 Rojas-Agramonte, Y., Kröner, A., Demoux, A., Xia, X., Wang, W., Donskaya, T., Liu,
617 D. & Sun, M., 2011. Detrital and xenocrystic zircon ages from Neoproterozoic to
618 Palaeozoic arc terranes of Mongolia: Significance for the origin of crustal
619 fragments in the Central Asian Orogenic Belt. Gondwana Research 19: 751-763.

620 Safonova, I., Maruyama, S., Hirata, T., Kon, Y. & Shuji Rino, S., 2010. LA ICP MS
621 U–Pb ages of detrital zircons from Russia largest rivers: Implications for major
622 granitoid events in Eurasia and global episodes of supercontinent formation.
623 Journal of Geodynamics 50, 134–153.
624 Seltmann, R. & Porter, T.M., 2005. The porphyry Cu–Au/Mo deposits of Central
625 Eurasia: 1. Tectonic, geologic and metallogenic setting and significant deposits.
626 In: Porter, T.M. (Ed.), Super Porphyry Copper and Gold Deposits: A Global
627 Perspective, vol. 2. PGC Publishing, Adelaide, 467–512.
628 Seltmann et al. Bipolar ages from zonal ongrowth of zircon at the Hugo Dummett Cu-
629 Au porphyry deposit (Oyu Tolgoi, Mongolia), Ore Geology Reviews, *in prep*.
630 Şengör, A.M.C., Natal'in, B.A., Burtman, V.S., 1993. Evolution of the Altaid tectonic
631 collage and Paleozoic crustal growth in Eurasia: Nature 364, 299–307.
632 Scherer E., Munker C. & Mezger K., 2001. Calibration of the Lutetium-Hafnium
633 clock. Science 293, 683-687.
634 Stacey, J.S. & Kramers, J.D., 1975. Approximation of terrestrial lead isotope
635 evolution by a two stage model. Earth and Planetary Science Letters 26 207–221.
636 Sun, S.S., McDonough, W.F., 1989. Chemical and isotopic systematics of oceanic
637 basalts: implications for mantel composition and processes. In: Saunders, A.D.,
638 Norry, M.J. (Eds.), Magmatism in ocean basins: Geological Society of London,
639 Special Publication, 42, pp. 313–342.
640 Taylor, S.R. & McLennan, S.M., 1985. The Continental Crust: its Composition and
641 Evolution. Blackwell Scientific Publications.
642 Wainwright, A. J., Tosdal, R. M., Wooden, J.L., Mazdab, F.K. & Friedman, R.M.,
643 2011. U–Pb (zircon) and geochemical constraints on the age, origin, and evolution
644 of Paleozoic arc magmas in the Oyu Tolgoi porphyry Cu–Au district, southern
645 Mongolia, Gondwana Research 19, 764–787.
646 Windley, B.F., Alexeiev, D., Xiao, W., Kröner, A. & Badarch, G., 2007. Tectonic
647 models for accretion of the Central Asian Orogenic Belt. Journal of the Geological
648 Society 164, 31–47.
649 Xiao, W.J., Pirajno, F. & Seltmann, R., 2008. Geodynamics and metallogeny of the
650 Altaid orogen. Journal of Asian Earth Sciences 32, 77-81.
651 Xiao, W., Windley, B.F., Huang, B.C., Han, C.M., Yuan, C., Chen, H.L., Sun, M.,
652 Sun, S. & Li, J.L., 2009. End-Permian to mid-Triassic termination of the
653 accretionary processes of the southern Altaids: implications for the geodynamic

evolution, Phanerozoic continental growth, and metallogeny of Central Asia. International Journal of the Earth Sciences 98 (6), 1189–1217.

Zartman, R.E., Doe, B.R., 1981. Plumbotectonics; the model. Tectonophysics 75, 135–162.

Appendix 1

Figure Captions

Figure 1. Tectonic setting of the Oyu Tolgoi porphyry Cu-Au deposits, Mongolia. The upper diagram illustrates the location of the Oyu Tolgoi deposit and the Gurvansayhan Terrane within the tectonic framework of Mongolia. After Kirwin et al. (2005), Ivanhoe Mines (2005), Wainwright et al. (2004) and references cited therein, Perello et al. (2001) and references cited therein (after Seltmann and~~&~~ Porter, 2005).

Figure 2. Regional geological setting of the Oyu Tolgoi porphyry Cu-Au deposits, Mongolia. The figure represents the outcrop geology surrounding the Oyu Tolgoi group of deposits. Sources same as in Fig. 1 (from Seltmann and~~&~~ Porter, 2005).

Figure 3. District scale geological setting of the Oyu Tolgoi porphyry Cu-Au deposits, Mongolia. The plan shows the interpreted solid sub-crop geology in the immediate vicinity of the deposits. Sources same as in Fig. 1 (from Seltmann and~~&~~ Porter, 2005).

Figure 4. General sample location map, showing pluton-sized intrusions.

Figure 5. Simplified geology of the Oyu Tolgoi Exploration Block and drill hole locations of samples included in this study.

Figure 6. Stratigraphy and location of samples included in this study (after Kavalieris, 2005).

Figure 7. Mantle-normalized multi-element diagram of the bulk rock samples from the study area (primitive mantle values are taken from McDonough and Sun, 1995).

Figure 8. Chondrite-normalized REE patterns of samples from the Oyu Tolgoi exploration block and adjacent areas; chondrite values taken from Sun and McDonough (1989).

Formatted: Font: Not Italic
Formatted: Font: Not Italic
Formatted: Font: Not Italic
Formatted: Font: Not Italic
Formatted: Font: Not Italic
Formatted: Font: Not Italic
Formatted: Font: Not Italic
Formatted: Font: Not Italic
Formatted: Font: Not Italic

Figure 9. Co-variation between the Sr and Nd parameters. The Nd data are considered more robust and show that all samples were derived from un-evolved sources typical of primitive island arcs.

Figure 10. εNd plotted versus the emplacement age of each body.

Figures 11 a, b. Results of zircon Hf isotope measurements for felsic igneous rocks from Oyu Tolgoi. a) Initial $^{176}Hf/^{177}Hf$ plotted against U-Pb age for individual zircon grains; compared to model lines for the evolution of deplted mantle and a chondritic reservoir (CHUR); b) Relative probability plot for the two-stage crustal residence ages calculated for each analysed spot.

Figures 12 a, b. Initial $^{207}Pb/^{204}Pb$ vs. $^{206}Pb/^{204}Pb$ and $^{208}Pb/^{204}Pb$ vs. $^{206}Pb/^{204}Pb$ plots showing results for plutonic and volcanic rocks from Oyu Tolgoi and surrounding areas. LC, lower crust; CC, continental crust; UC, upper crust; OR, orogene; M, mantle (from Zartman and Doe, 1981).

Formatted: Font: Not Italic

Figure 13. εHf and εNd data plotted for the South Gobi area (compilation of the CERCAMS Altaids project) and samples of this study.

Formatted: Font: Not Italic

Note: strongly crustal: εHf <-5, εNd(t) <-7; crustal: εHf -5 to 0, εNd(t) -7 to -2; mixed: εHf 0 to +5, εNd(t) -2 to 0; juvenile: εHf +5 to +10, εNd(t) 0 to +5; strongly juvenile: εHf >+10, εNd(t) >+5.

Table and Appendix C~~c~~aptions

Table 1. Sample list with U-Pb zircon ages of samples from the study area (Kavalieris, 2005; Seltmann et al., in preparation).

Table 2. Whole rock geochemical data for samples from the Oyu Tolgoi exploration block and adjacent areas.

Table 3. Sm and Nd isotope data for samples from the Oyu Tolgoi exploration block and adjacent areas.

Table 4. Lu-Hf isotope analyses of U–Pb dated zircon grains.

Table 5. Pb isotope data for samples from the Oyu Tolgoi exploration block and adjacent areas.

Appendix 1. Mineralogical description of studied samples.

Formatted: Font: Not Italic

Formatted: Font: Bold

Formatted: Font: Not Bold

Formatted: Font: Not Bold

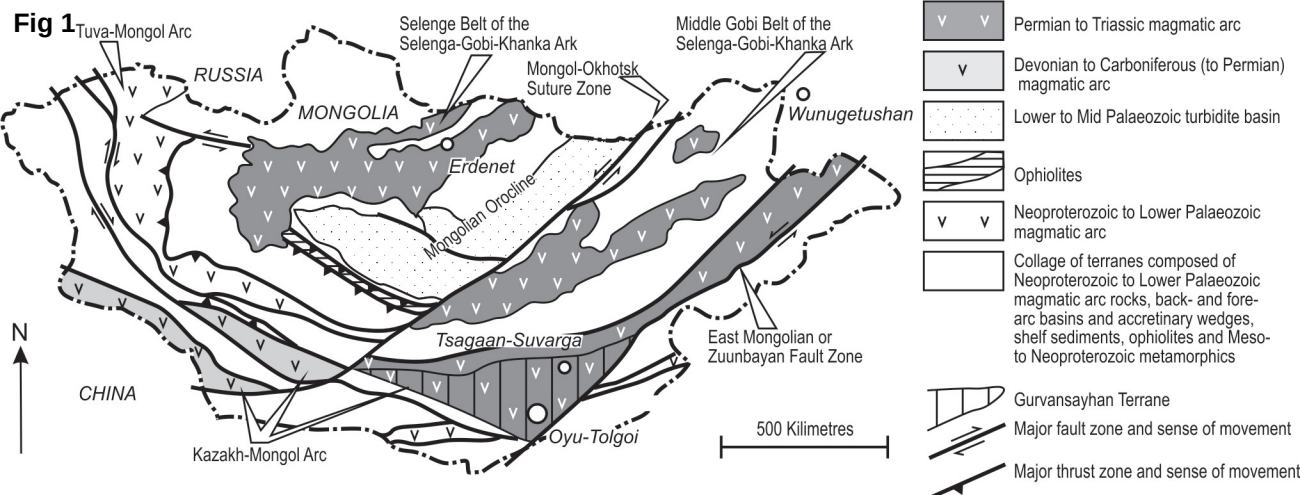
Fig 1
Tuva-Mongol Arc
Selenge Belt of the Selenga-Gobi-Khanka Ark
Middle Gobi Belt of the Selenga-Gobi-Khanka Ark
RUSSIA
MONGOLIA
Mongol-Okhotsk Suture Zone
Wunugetushan
Erdenet
Mongolian Orocline
Tsagaan-Suvarga
East Mongolian or Zuunbayan Fault Zone
CHINA
Oyu-Tolgoi
Kazakh-Mongol Arc
N
500 Kilometres
Permian to Triassic magmatic arc
Devonian to Carboniferous (to Permian) magmatic arc
Lower to Mid Palaeozoic turbidite basin
Ophiolites
Neoproterozoic to Lower Palaeozoic magmatic arc
Collage of terranes composed of Neoproterozoic to Lower Palaeozoic magmatic arc rocks, back- and fore-arc basins and accretinary wedges, shelf sediments, ophiolites and Meso- to Neoproterozoic metamorphics
Gurvansayhan Terrane
Major fault zone and sense of movement
Major thrust zone and sense of movement

Figure 1

Figure 2

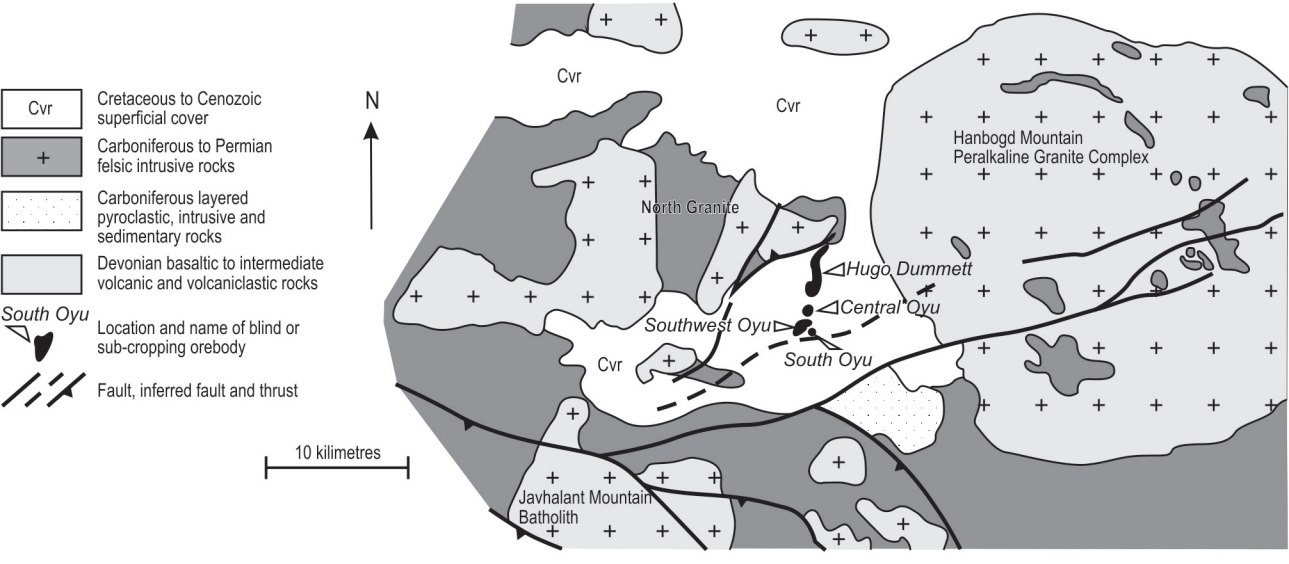
Cvr
Cretaceous to Cenozoic superficial cover
Carboniferous to Permian felsic intrusive rocks
Carboniferous layered pyroclastic, intrusive and sedimentary rocks
Devonian basaltic to intermediate volcanic and volcaniclastic rocks
South Oyu
Location and name of blind or sub-cropping orebody
Fault, inferred fault and thrust
N
10 kilometres
Cvr
Cvr
Cvr
Hanbogd Mountain
Peralkaline Granite Complex
North Granite
Hugo Dummett
Central Oyu
Southwest Oyu
South Oyu
Javhalant Mountain
Batholith

Figure 3

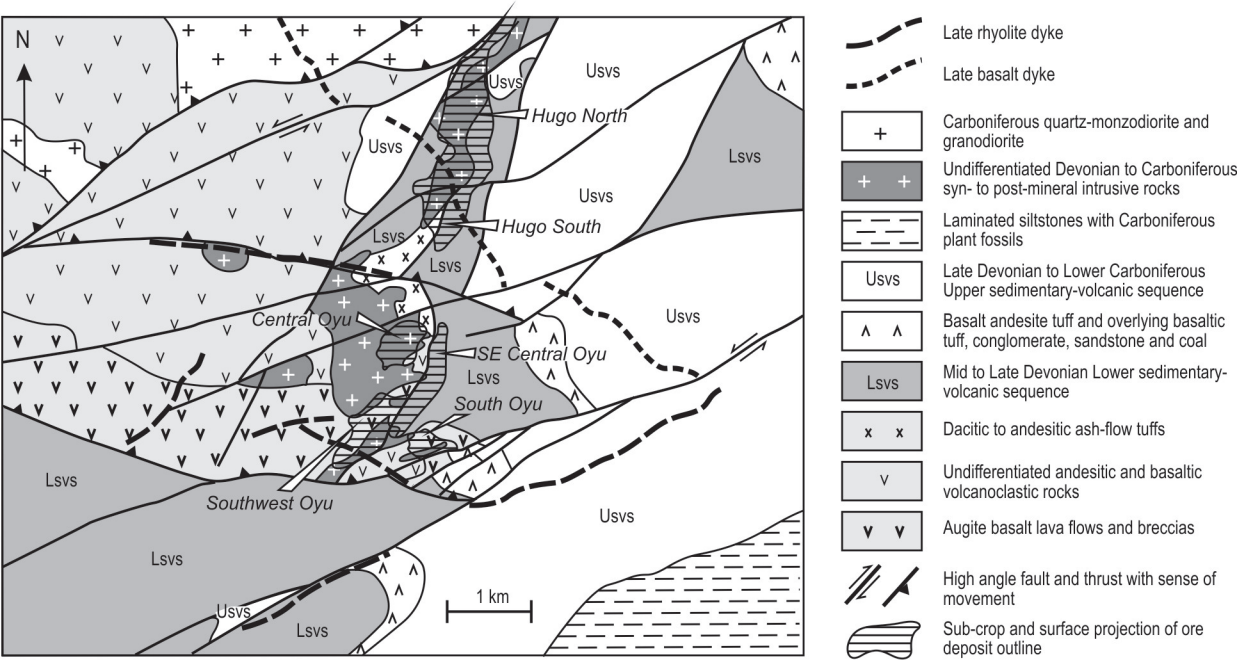
N
Usvs
Hugo North
Hugo South
Lsvs
Central Oyu
SE Central Oyu
South Oyu
Southwest Oyu
1 km
Late rhyolite dyke
Late basalt dyke
Carboniferous quartz-monzodiorite and granodiorite
Undifferentiated Devonian to Carboniferous syn- to post-mineral intrusive rocks
Laminated siltstones with Carboniferous plant fossils
Late Devonian to Lower Carboniferous Upper sedimentary-volcanic sequence
Basalt andesite tuff and overlying basaltic tuff, conglomerate, sandstone and coal
Mid to Late Devonian Lower sedimentary-volcanic sequence
Dacitic to andesitic ash-flow tuffs
Undifferentiated andesitic and basaltic volcanoclastic rocks
Augite basalt lava flows and breccias
High angle fault and thrust with sense of movement
Sub-crop and surface projection of ore deposit outline

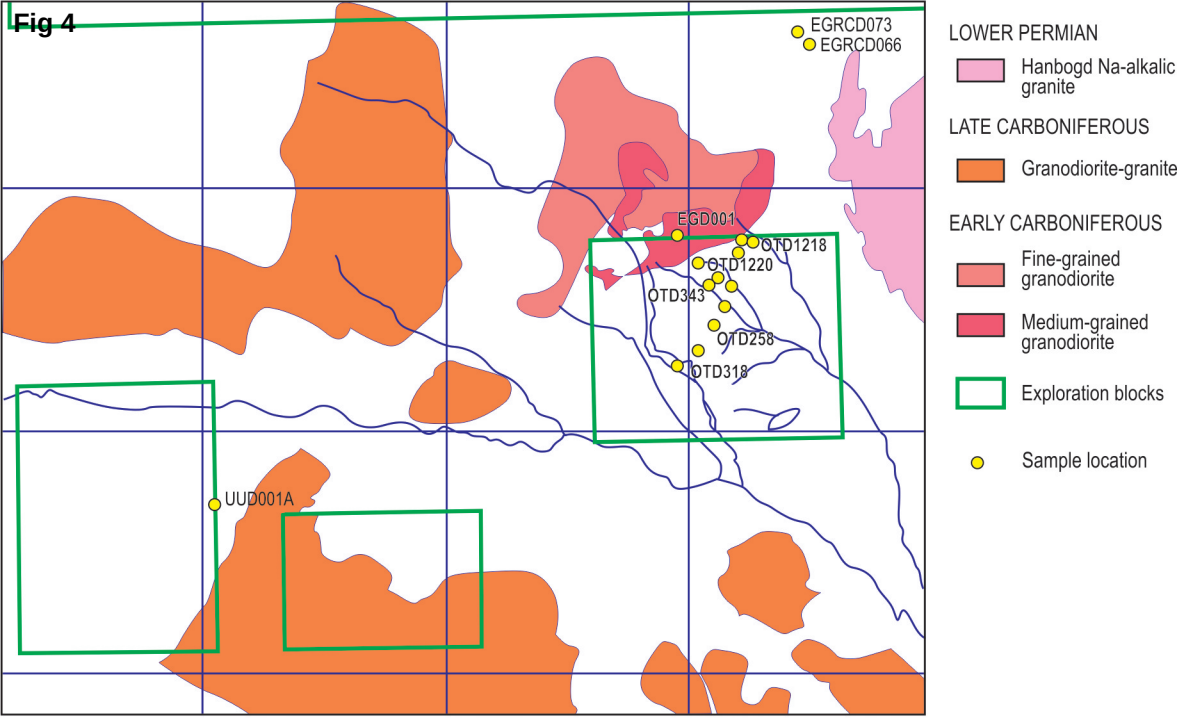
Fig 4
EGRCD073
EGRCD066
EGD001
OTD1218
OTD1220
OTD343
OTD258
OTD318
UUD001A
LOWER PERMIAN
Hanbogd Na-alkalic granite
LATE CARBONIFEROUS
Granodiorite-granite
EARLY CARBONIFEROUS
Fine-grained granodiorite
Medium-grained granodiorite
Exploration blocks
Sample location

Figure 4

Fig 5

Figure 5

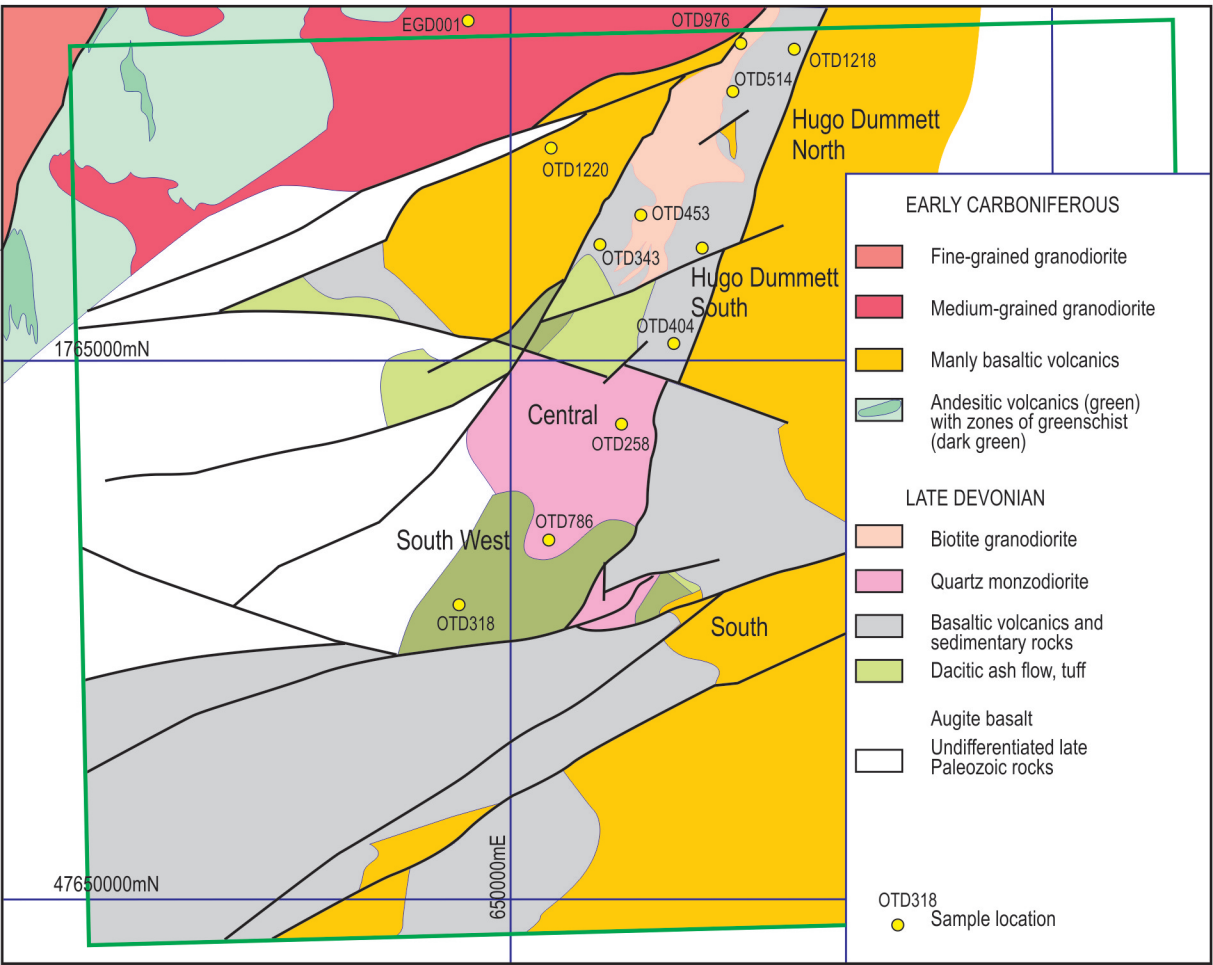

Fig 6

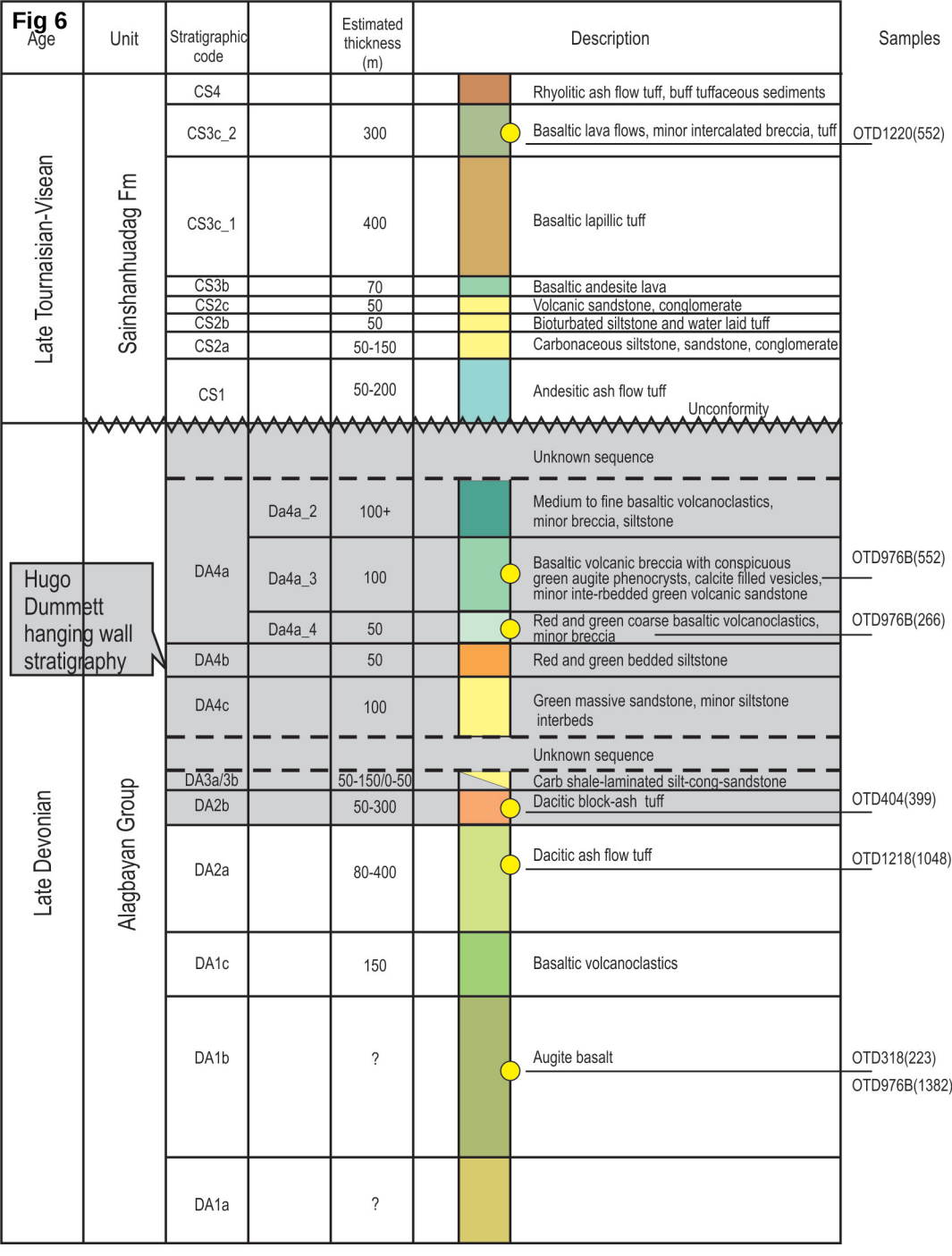

Figure 6

Fig 7

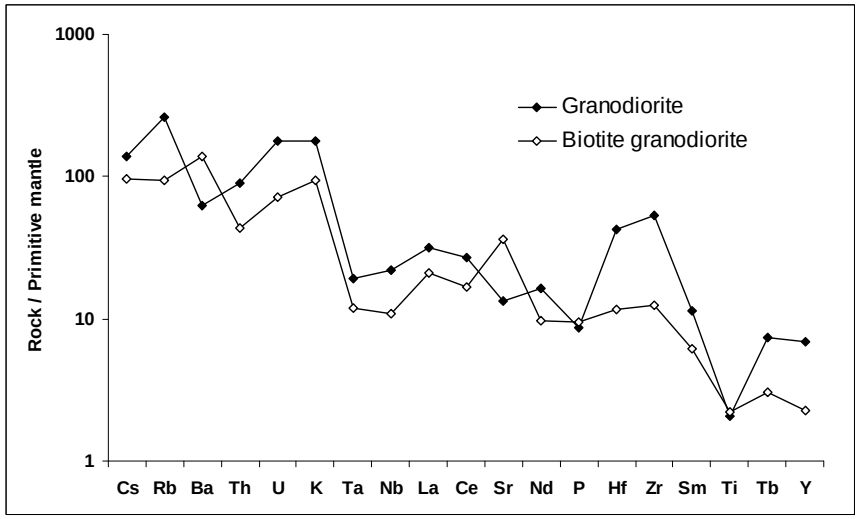

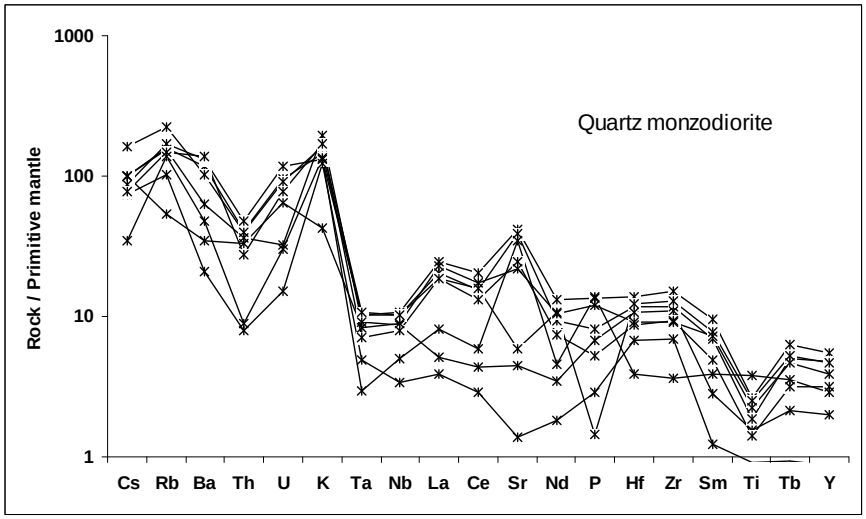

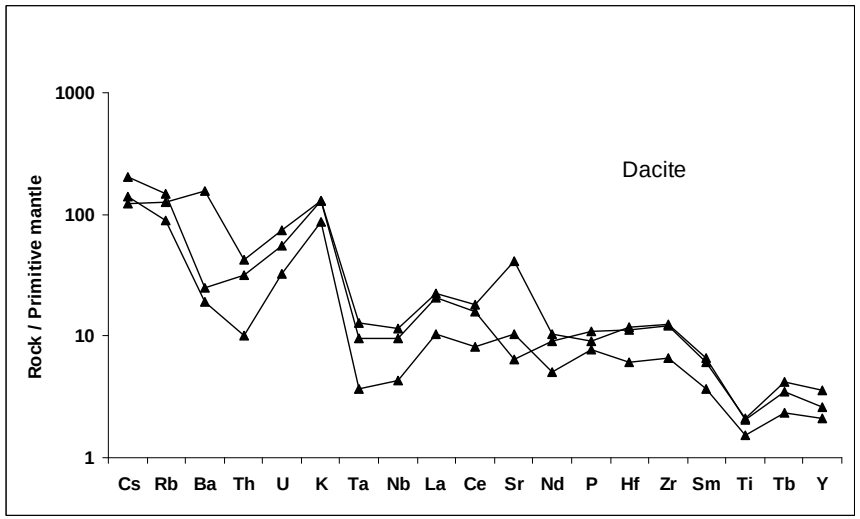

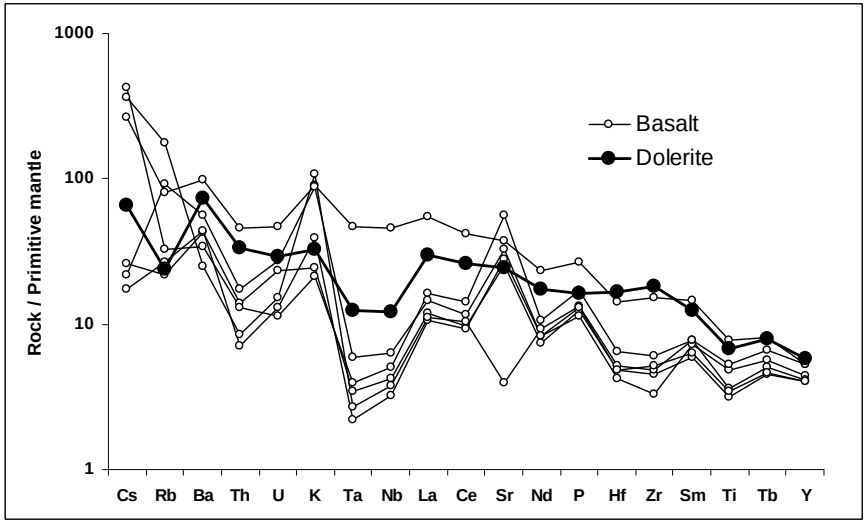

Figure 7

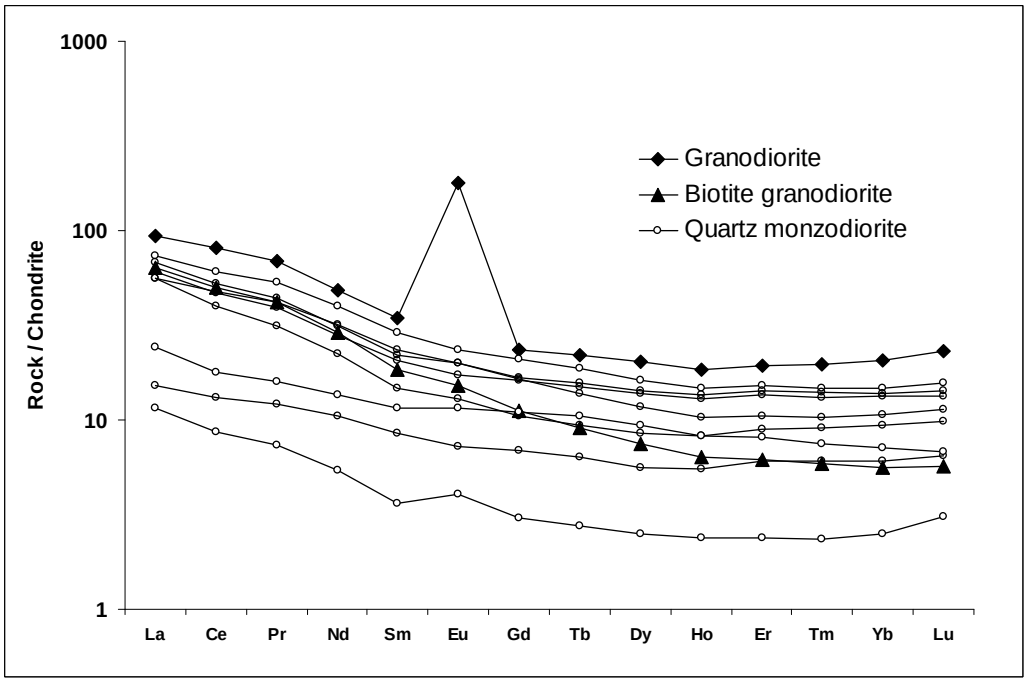
1000
100
10
1
Rock / Chondrite
Granodiorite
Biotite granodiorite
Quartz monzodiorite
La
Ce
Pr
Nd
Sm
Eu
Gd
Tb
Dy
Ho
Er
Tm
Yb
Lu

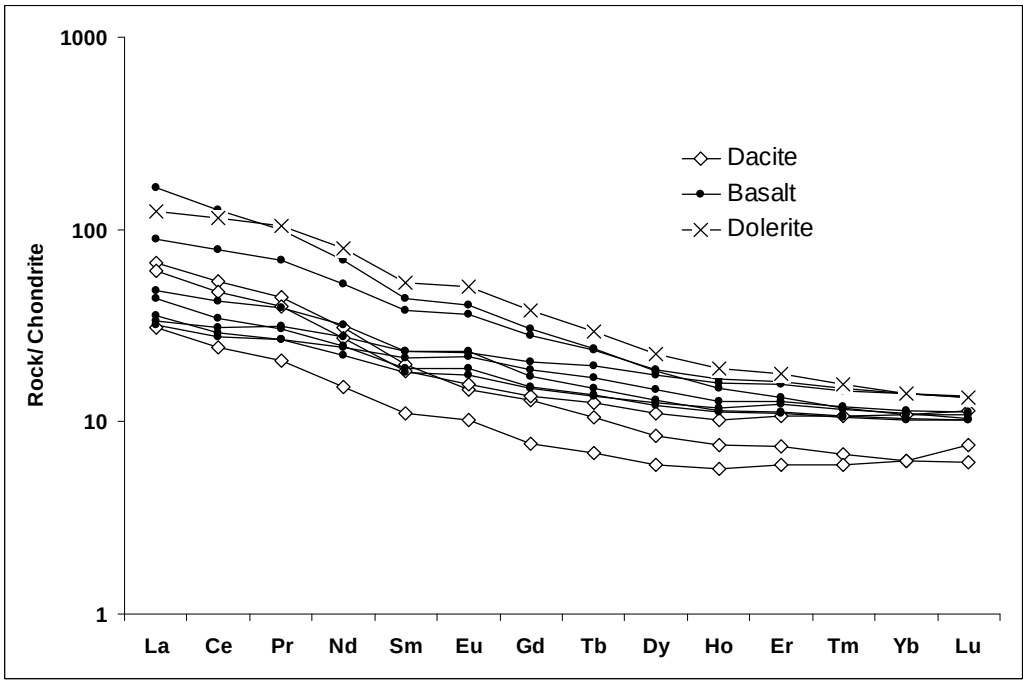
1000
100
10
1
Rock/ Chondrite
Dacite
Basalt
Dolerite
La
Ce
Pr
Nd
Sm
Eu
Gd
Tb
Dy
Ho
Er
Tm
Yb
Lu

Figure 8

Fig 9

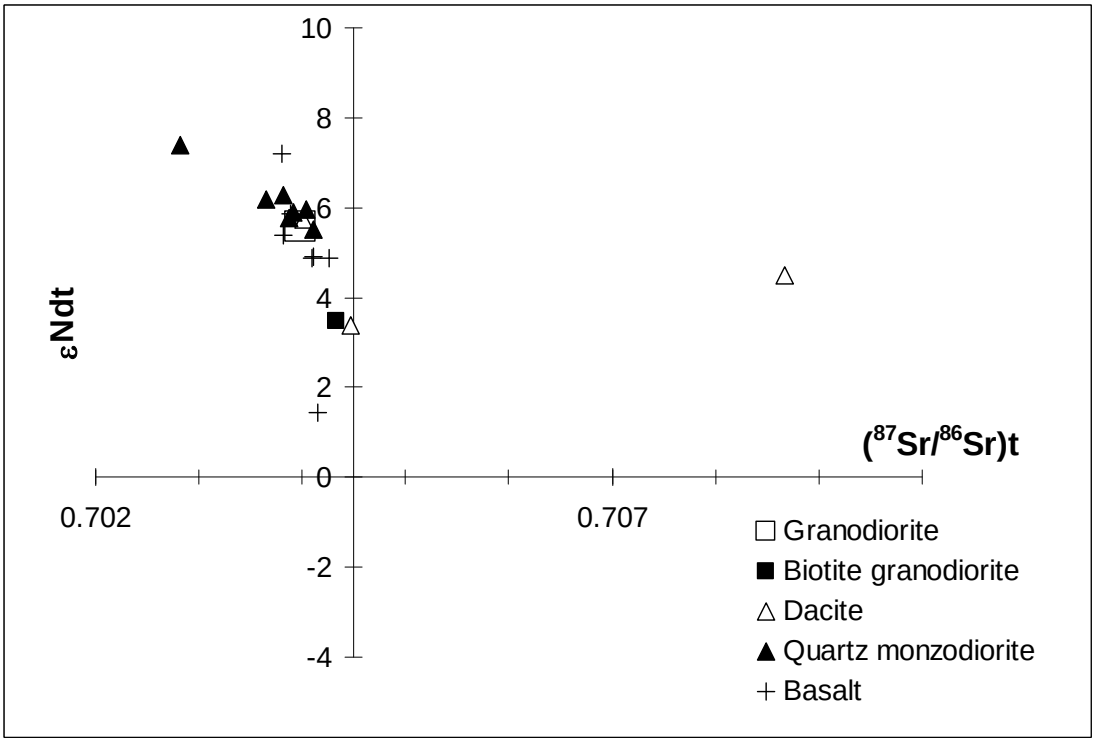

Figure 9

Fig 10

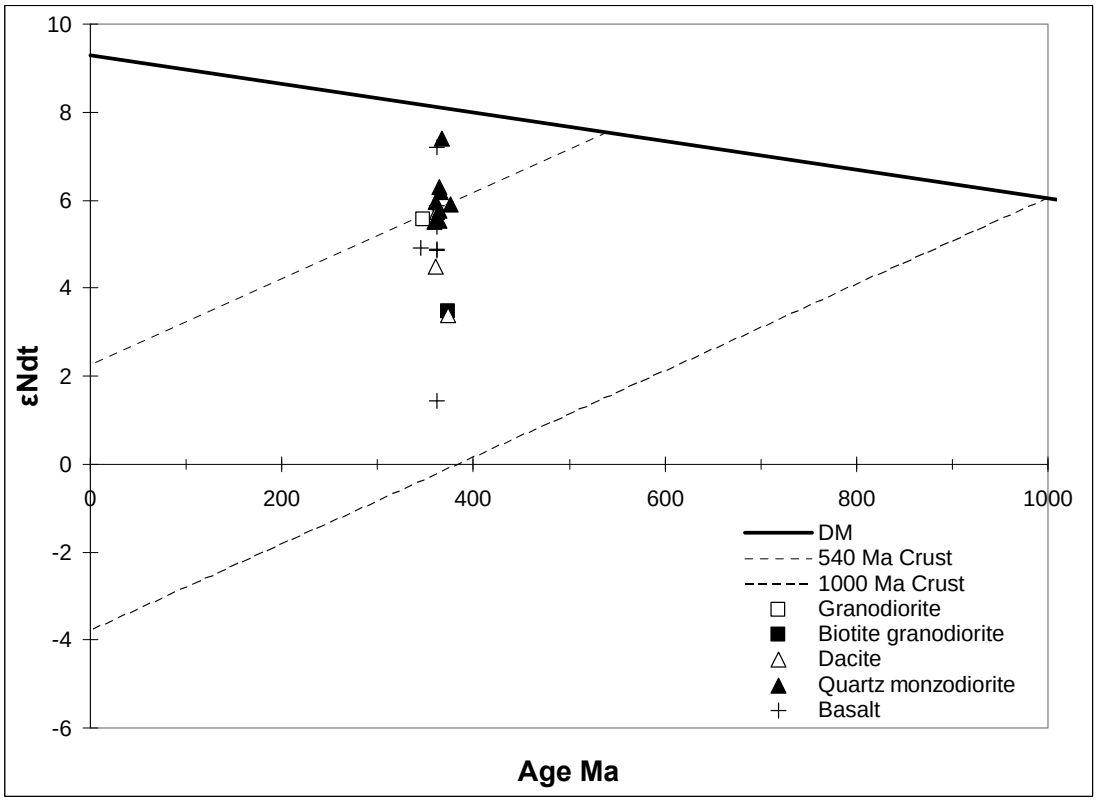

Figure 10

Fig 11

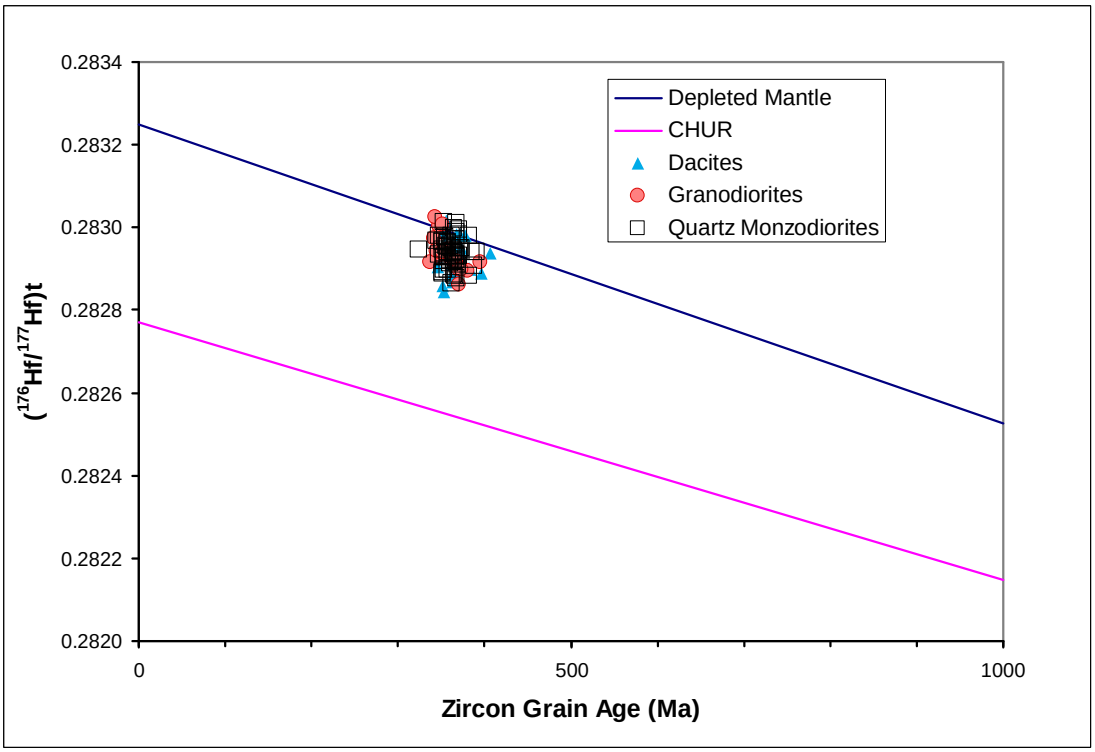

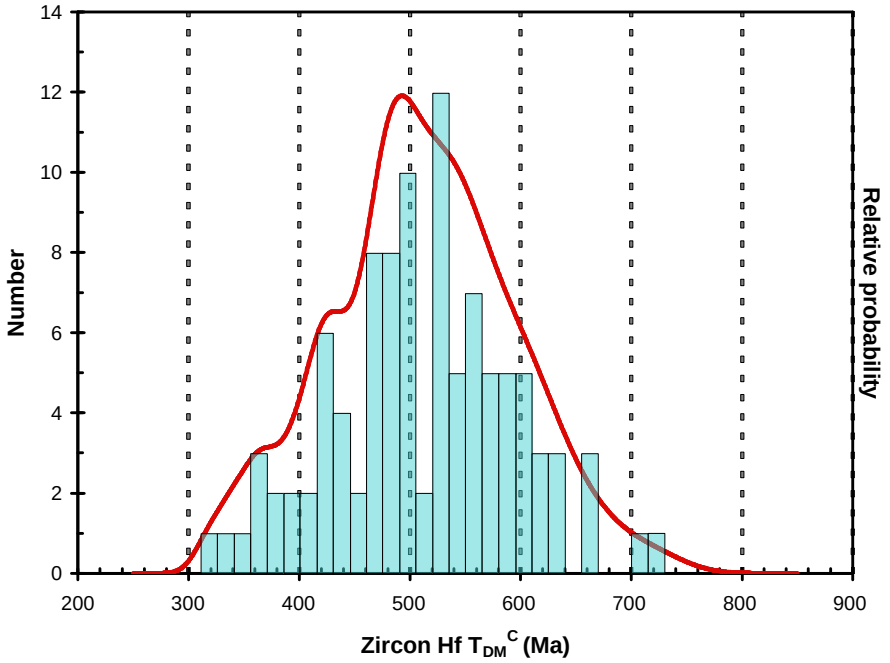

Figures 11a, b

Fig 12

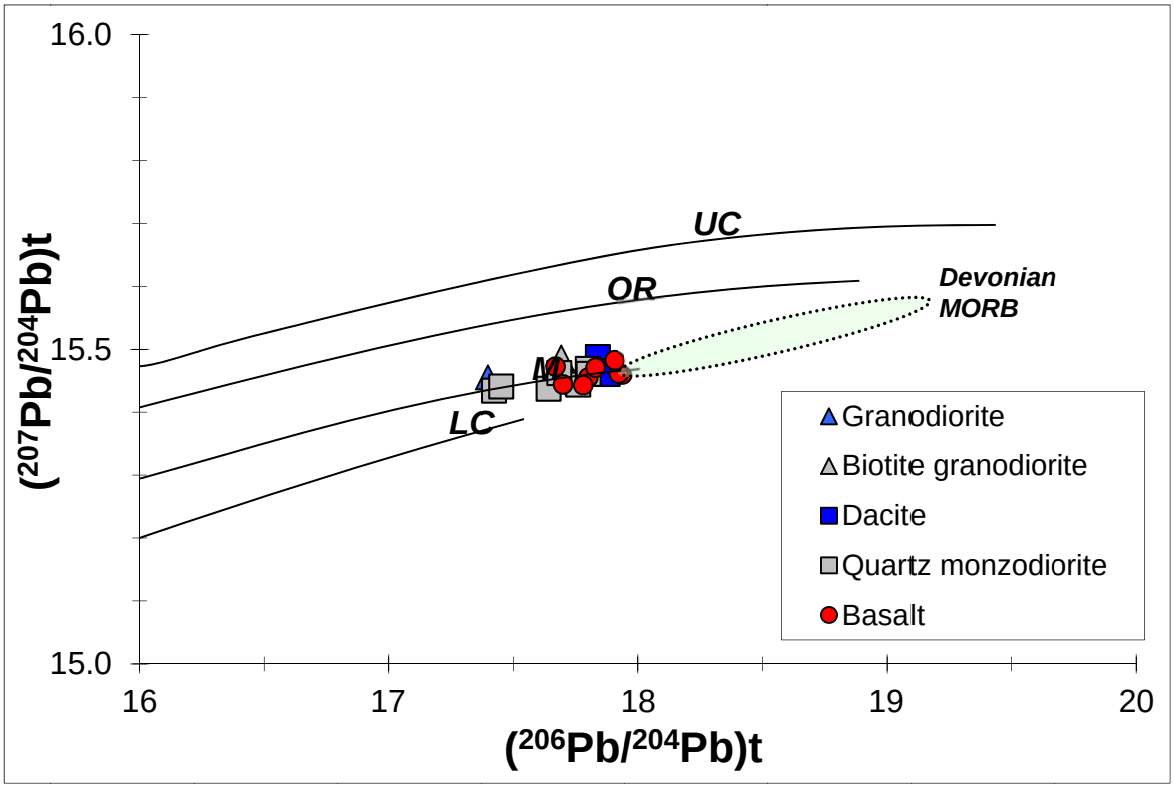

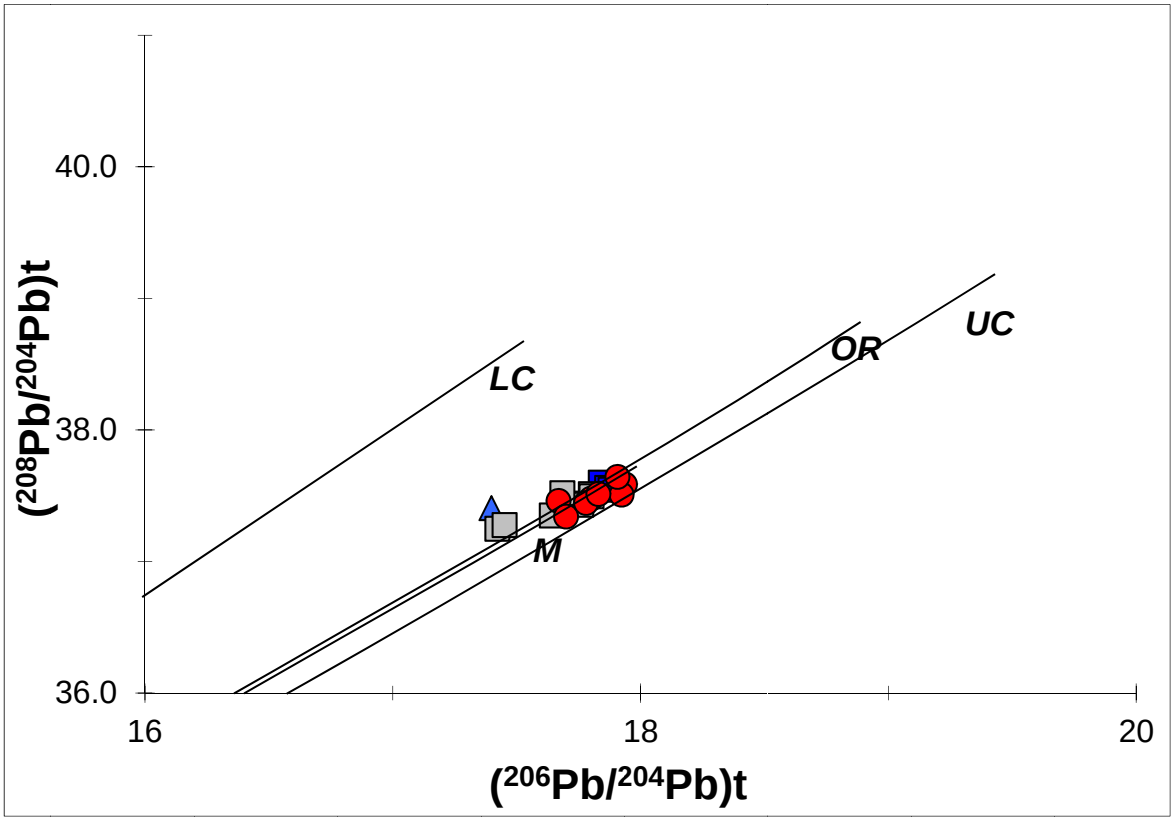

Figure 12 a, b

Fig 13

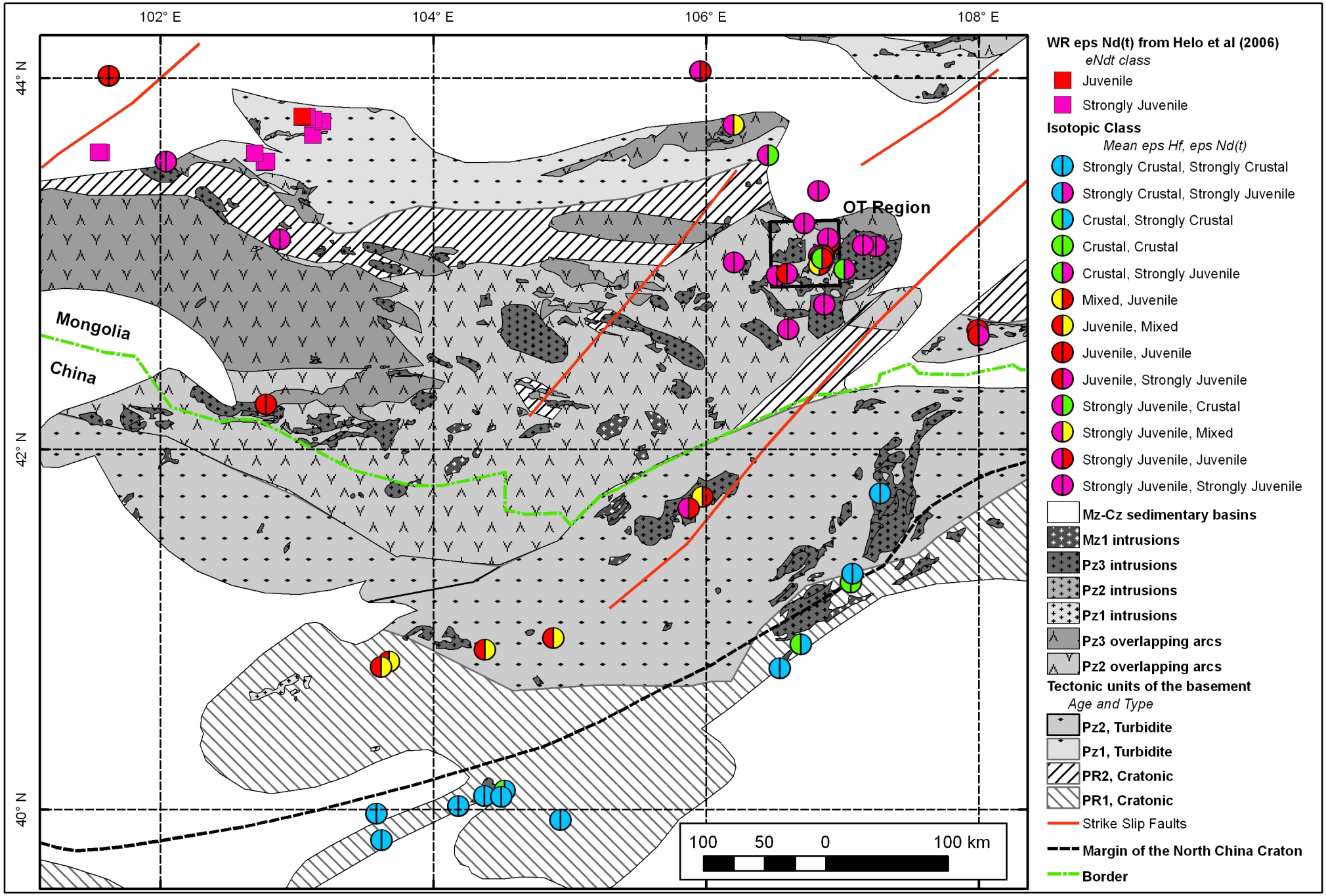
102° E
104° E
106° E
108° E
44° N
42° N
40° N
Mongolia
China
OT Region
100 50 0 100 km
WR eps Nd(t) from Helo et al (2006)
eNdt class
Juvenile
Strongly Juvenile
Isotopic Class
Mean eps Hf, eps Nd(t)
Strongly Crustal, Strongly Crustal
Strongly Crustal, Strongly Juvenile
Crustal, Strongly Crustal
Crustal, Crustal
Crustal, Strongly Juvenile
Mixed, Juvenile
Juvenile, Mixed
Juvenile, Juvenile
Juvenile, Strongly Juvenile
Strongly Juvenile, Crustal
Strongly Juvenile, Mixed
Strongly Juvenile, Juvenile
Strongly Juvenile, Strongly Juvenile
Mz-Cz sedimentary basins
Mz1 intrusions
Pz3 intrusions
Pz2 intrusions
Pz1 intrusions
Pz3 overlapping arcs
Pz2 overlapping arcs
Tectonic units of the basement
Age and Type
Pz2, Turbidite
Pz1, Turbidite
PR2, Cratonic
PR1, Cratonic
Strike Slip Faults
Margin of the North China Craton
Border

Table 1
Click here to download Table: Table 1.xls

Table 1

#	Sample Nr	Lithology	Age	Coordinates		$^{206}Pb/^{238}U$ age (Ma)	Note
				Latitude	Longitude		
1	**EGD001(75)**	Granodiorite	348	43.0515	106.8365	348±4	1
2	**OTD514(1631.2-1631.7)**	Biotite granodiorite	374	43.0458	106.8609	374±4	1
3	**EGRDC066(172)**	Dacite	374	43.1208	106.9055	374±12	2
4	**OTD1218(1048-1048.8)**	Dacite	361	43.0508	106.869	361±5	1
5	**OTD404(399)**	Dacite	362	43.0247	106.858	362±7	1
6	**EGRCD073(120)**	Quartz monzodiorite	361	43.1434	106.8999	361±4	1
7	**OTRCD388(504)**	Quartz monzodiorite	364	43.0324	106.8617	(362)	3
8	**OTD258(82.5)**	Quartz monzodiorite	359	43.017	106.8533	359±8	1
9	**OTD343(1247)**	Quartz monzodiorite	366	43.0295	106.8555	366±6	1
10	**OTD514(1289.15-1293.7)**	Quartz monzodiorite	364	43.0454	106.8622	364±6	1
11	**OTD514(1405.85-1410.15)**	Quartz monzodiorite	367	43.0562	106.8617	367±7	1
12	**OTD514(2161.35)**	Quartz monzodiorite	364	43.0465	106.8592	364±5	1
13	**OTD786(150)**	Quartz monzodiorite	376	43.0075	106.8452	376±4	1
15	**OTD976B(266-267)**	Basalt	362	43.049	106.8677	(362)	3
16	**OTD976B(552)**	Basalt	362	43.049	106.8672	(362)	3
17	**0TB976B(772)**	Basalt dyke	362	43.0489	106.8672	(362)	3
14	**OTD976B(1382.5-1383.5)**	Basalt	362	43.0488	106.8654	(362)	3
18	**UUDO1A(590-593)**	Basalt	362	42.9543	106.597	(362)	3
19	**OTD1220(522)**	Basalt	345	43.0404	106.8488	(345)	3
20	**OTD318(223)**	Basalt	362	43.0019	106.8345	(362)	3

1 – Preferred crystallisation age, 2 – minimum age, supported from other geological and geochronological data, 3 – the estimated ages of the basalts are inferred from their stratigraphic position and by comparison with the dated dacites; the age for OTRCD 388 is also assumed.

Table 2

Click here to download Table: Table 2.xls

Table 2

Element	Unit	EGD	OTD	EGRCD	OTD	OTD	EGRCD	OTRCD	OTD	OTD	OTD	OTD	OTD	OTD	OTD	OTD	OTD	UUD	OTD	OTD	OTD
		001(75)	514(1631)	066(172)	1218(1048)	404(399)	073(120)	388(504)	258(82)	343(1247)	514(1289)	514(1405)	514(2161)	786(150)	976B(266)	976B(552)	976B(772)	976B(1382)	001A(590)	1220(552)	318(223)	453(367)
SiO2	%	62.77	63.73	66.12	67.42	67.47	60.23	68.91	68.9	59.23	70.98	68.6	65.13	59.45	42.96	48.83	49.32	46.28	48.14	48.54	44.99	50.93
Al2O3	%	16.66	15.19	15.91	16.47	15.68	17.84	13.14	16.42	17.12	13.01	13.75	16.01	16.75	14.26	18.08	14.97	15.67	15.16	13.43	15.7	15.65
Fe2O3(T)	%	4.86	3.8	3.61	3.83	3.3	5.8	3.98	4.38	7.91	2.94	3.35	2.91	4.77	11.6	8.73	10.59	11.6	9.72	10.35	12.53	10.14
MnO	%	0.124	0.07	0.113	0.047	0.081	0.052	0.012	0.016	0.121	0.015	0.048	0.038	0.135	0.2	0.209	0.175	0.219	0.118	0.163	0.224	0.179
MgO	%	0.9	1.89	1.07	0.95	0.51	1.56	0.49	0.54	1.38	0.47	0.97	0.56	1.43	4.98	3.76	5.78	8.85	5.13	6.62	7.46	4.74
CaO	%	2.29	2.97	2.57	0.95	2.02	3.43	0.17	0.13	0.26	0.1	0.84	2.41	4.14	9	5.3	9.74	3.43	6.75	11.26	10.47	4.76
Na2O	%	4.53	4.6	3.98	1.84	4.53	4.33	0.11	0.5	0.25	0.2	0.22	4.18	6.85	1.66	5.46	2.84	0.72	4.83	3.25	2.5	4.9
K2O	%	5.13	2.75	3.75	3.75	2.49	4.15	3.91	3.79	4.69	3.59	5.65	4.87	1.23	2.6	0.62	2.53	3.12	0.95	0.71	1.14	2.81
TiO2	%	0.439	0.472	0.439	0.444	0.323	0.556	0.807	0.396	0.533	0.193	0.331	0.305	0.479	1.64	0.771	0.743	1.138	1.431	0.669	1.032	2.346
P2O5	%	0.18	0.2	0.19	0.23	0.16	0.28	0.29	0.17	0.03	0.06	0.14	0.11	0.25	0.56	0.36	0.27	0.28	0.34	0.26	0.24	1.19
LOI	%	1.54	3.86	1.46	3.54	3.27	2.12	3.41	4.99	7.02	2.46	3.5	3.34	4.68	9.15	6.54	3.12	7.79	6.88	4.32	3.54	2.48
Total	%	99.43	99.53	99.21	99.46	99.85	100.3	95.23	100.2	98.54	94.02	97.41	99.88	100.2	98.61	98.66	100.1	99.11	99.45	99.58	99.83	100.1
Sc	ppm	8	7	6	6	4	7	13	5	6	2	4	3	6	35	17	37	31	30	40	40	23
Be	ppm	3	2	2	2	1	2	< 1	2	2	< 1	1	2	2	3	2	2	2	2	2	2	3
V	ppm	34	75	64	76	81	147	172	89	116	61	63	95	124	261	243	296	333	244	271	417	227
Cr	ppm	< 20	30	60	< 20	< 20	< 20	30	< 20	< 20	< 20	< 20	< 20	< 20	30	30	90	90	490	180	80	< 20
Co	ppm	6	8	8	4	4	9	3	7	14	8	4	2	8	36	27	35	33	41	36	43	20
Ni	ppm	< 20	< 20	30	< 20	< 20	< 20	< 20	< 20	< 20	< 20	< 20	< 20	< 20	< 20	< 20	20	< 20	200	30	40	< 20
Cu	ppm/%	40	50	100	110	60	4520	3.26%	210	1070	4.62%	2.82%	1360	130	120	50	340	650	50	130	200	40
Zn	ppm	70	80	110	70	50	40	60	120	260	100	90	50	90	120	100	90	250	110	80	150	140
Ga	ppm	20	20	19	18	18	20	11	23	20	13	15	18	17	20	20	17	18	17	15	20	21
Ge	ppm	1.8	1.3	1.3	1.5	1.5	1.8	2.5	1.5	1.3	2	1.6	1.5	2.5	1.6	1.6	2.1	1.7	2.4	2.5	2	1.4
As	ppm	< 5	< 5	7	12	15	6	7	197	53	170	77	< 5	24	45	29	32	< 5	37	40	21	35
Rb	ppm	166	60	80	95	56	101	88	107	143	65	98	94	34	51	21	59	112	15	14	17	47
Sr	ppm	280	771	868	134	217	876	728	815	125	29	95	514	457	792	1185	694	83	516	544	592	1420
Y	ppm	31.7	10.4	11.8	16.5	9.5	25.2	13	21.7	21.3	4	9.1	14.4	17.5	24	18.8	18.5	23.8	26.2	18.4	20.1	29.5
Zr	ppm	597	139	141	135	73	170	41	133	145	77	122	105	103	170	68	58	54	203	51	37	245
Nb	ppm	15.6	7.7	8.3	6.9	3.1	7.7	3.6	7.3	7.3	2.4	6.2	5.6	6.4	32.8	3.6	4.5	2.7	8.6	3	2.3	12.6
Mo	ppm	< 2	< 2	< 2	< 2	< 2	41	8	2	48	13	8	73	< 2	< 2	< 2	< 2	< 2	< 2	< 2	< 2	< 2
Ag	ppm	< 0.5	0.8	< 0.5	< 0.5	< 0.5	< 0.5	0.8	< 0.5	< 0.5	11.3	1.3	< 0.5	< 0.5	< 0.5	< 0.5	< 0.5	< 0.5	0.5	< 0.5	< 0.5	< 0.5
In	ppm	< 0.1	< 0.1	< 0.1	< 0.1	< 0.1	< 0.1	0.1	< 0.1	< 0.1	0.3	< 0.1	< 0.1	< 0.1	< 0.1	< 0.1	< 0.1	< 0.1	< 0.1	< 0.1	< 0.1	< 0.1
Sn	ppm	1	1	25	< 1	< 1	< 1	2	< 1	1	2	< 1	< 1	< 1	< 1	< 1	< 1	< 1	1	< 1	< 1	1
Sb	ppm	7.7	7.9	22.1	11.6	15.1	8.1	8.9	11.5	6.9	3.7	62	8.4	11	7.7	11.7	9.7	9.4	9.2	10.8	1	9.5
Cs	ppm	3.2	2.2	2.8	4.7	3.2	2.3	0.8	2	3.7	1.7	2.3	1.8	2.3	6.1	9.8	0.5	8.3	1.5	0.6	0.4	1
Ba	ppm	442	964	1080	174	134	829	335	926	723	147	443	971	244	683	239	396	176	512	302	307	1481
La	ppm	22.3	15	16	14.5	7.31	17.4	5.71	14.4	13.3	2.76	3.6	13.2	16.2	39.2	11.4	10.3	7.91	21	8.44	7.51	29.2
Ce	ppm	49.7	30.8	33	28.9	14.9	37	10.9	28.7	29.3	5.33	8.07	24.4	32	77.3	25.8	21.3	19	48.1	17.8	16.9	70.1
Pr	ppm	6.38	3.87	4.13	3.69	1.92	4.97	1.47	3.63	3.92	0.68	1.12	2.93	4.1	9.23	3.64	2.82	2.93	6.41	2.49	2.47	9.67
Nd	ppm	22.3	13.3	14.1	12.5	6.9	18.2	6.22	12.8	14.6	2.49	4.76	10.2	14.4	31.6	14.5	11.3	12.6	23.8	10.2	11.2	36.6
Sm	ppm	5.08	2.72	2.94	2.73	1.63	4.27	1.72	3.04	3.46	0.54	1.26	2.18	3.24	6.46	3.46	2.8	3.43	5.57	2.65	3.2	7.88
Eu	ppm	10.1	0.859	0.831	0.876	0.571	1.32	0.651	0.974	1.12	0.227	0.41	0.734	1.13	2.27	1.31	1.06	1.28	2.05	0.977	1.23	2.84
Gd	ppm	4.7	2.24	2.57	2.72	1.53	4.18	2.19	3.21	3.33	0.6	1.37	2.09	3.26	6.03	3.44	3.02	4.05	5.55	2.95	3.73	7.53
Tb	ppm	0.8	0.33	0.38	0.45	0.25	0.68	0.38	0.54	0.57	0.1	0.23	0.34	0.5	0.87	0.54	0.5	0.71	0.85	0.49	0.61	1.07
Dy	ppm	4.96	1.83	2.09	2.71	1.47	3.99	2.29	3.38	3.53	0.62	1.37	2.11	2.87	4.5	3.17	3	4.28	4.61	3.08	3.6	5.58
Ho	ppm	1.01	0.35	0.41	0.56	0.31	0.8	0.45	0.71	0.74	0.13	0.3	0.45	0.56	0.81	0.62	0.61	0.87	0.91	0.64	0.7	1.04
Er	ppm	3.09	0.99	1.2	1.71	0.96	2.42	1.3	2.17	2.27	0.38	0.97	1.43	1.68	2.15	1.81	1.76	2.51	2.58	1.96	2.04	2.86
Tm	ppm	0.483	0.146	0.168	0.263	0.147	0.363	0.186	0.327	0.344	0.058	0.149	0.225	0.255	0.29	0.265	0.259	0.358	0.369	0.285	0.296	0.384
Yb	ppm	3.32	0.9	1	1.75	1.01	2.37	1.15	2.15	2.21	0.4	0.98	1.5	1.71	1.76	1.66	1.64	2.24	2.25	1.78	1.85	2.26
Lu	ppm	0.568	0.139	0.151	0.281	0.186	0.384	0.167	0.328	0.35	0.076	0.159	0.242	0.282	0.268	0.253	0.253	0.333	0.33	0.256	0.278	0.328
Hf	ppm	13.2	3.6	3.7	3.5	1.9	4.3	1.2	3.6	3.8	2.1	3.3	2.7	2.8	4.4	2	1.5	1.6	5.1	1.5	1.3	5.5
Ta	ppm	0.79	0.49	0.53	0.39	0.15	0.42	0.12	0.42	0.44	0.2	0.37	0.29	0.34	1.94	0.16	0.24	0.11	0.51	0.14	0.09	0.7
W	ppm	< 0.5	4.1	1.8	1.3	< 0.5	4	3.4	< 0.5	4.8	1.8	3.4	3.8	2	< 0.5	< 0.5	< 0.5	< 0.5	< 0.5	< 0.5	0.5	< 0.5
Tl	ppm	0.63	0.2	0.49	0.87	0.51	0.3	2.14	1.66	1.43	0.92	0.68	0.4	0.19	0.18	0.09	0.13	1.29	0.11	< 0.05	0.1	0.31
Pb	ppm	8	8	23	10	8	< 5	53	30	< 5	93	32	< 5	12	5	< 5	6	12	7	< 5	8	16
Bi	ppm	0.1	0.1	0.4	0.3	0.1	0.7	0.6	0.3	0.1	2.3	0.6	< 0.1	0.9	< 0.1	0.1	0.1	0.1	0.2	< 0.1	< 0.1	< 0.1
Th	ppm	7.54	3.67	3.54	2.64	0.84	3.39	0.75	4.03	3.33	0.67	3.08	2.32	2.79	3.81	1.1	1.47	0.72	2.78	1.17	0.6	2.25
U	ppm	3.74	1.51	1.57	1.17	0.68	2	0.64	2.48	1.92	0.32	0.68	1.64	1.37	0.99	0.24	0.57	0.32	0.62	0.49	0.27	0.73

Table 3

Click here to download Table: Table 3_NdSr.xls

Table 3

#	Sample Nr	Lithology	Age	$^{147}Sm/^{144}Nd$	$^{143}Nd/^{144}Nd$	$^{143}Nd/^{144}Ndt$	εNdt	Tdm	Tdm*	$^{87}Rb/^{86}Sr$	$^{87}Sr/^{86}Sr$	$^{87}Sr/^{86}Srt$
1	**EGD001(75)**	Granodiorite	348	0.13773	0.512789	0.51247	5.6	589	600	1.716	0.712480	0.7040
2	**OTD514(1631.2-1631.7)**	Biotite granodiorite	374	0.12364	0.512637	0.51233	3.5	739	822	0.225	0.705528	0.7043
3	**EGRDC066(172)**	Dacite	374	0.12606	0.512638	0.51233	3.4	756	831	0.267	0.705885	0.7045
4	**OTD1218(1048-1048.8)**	Dacite	361	0.13204	0.512715	0.51240	4.5	676	716	2.054	0.719224	0.7087
5	**OTD404(399)**	Dacite	362	0.14282	0.512804	0.51247	5.7	597	593	0.747	0.707855	0.7040
6	**EGRCD073(120)**	Quartz monzodiorite	361	0.14184	0.512814	0.51248	6.0	572	570	0.334	0.705754	0.7040
7	**OTRCD388(504)**	Quartz monzodiorite	364	0.16719	0.512890	0.51249	6.3	624	538	0.350	0.705627	0.7038
8	**OTD258(82.5)**	Quartz monzodiorite	359	0.14359	0.512796	0.51246	5.5	620	614	0.380	0.706051	0.7041
9	**OTD343(1247)**	Quartz monzodiorite	366	0.14328	0.512827	0.51248	6.2	557	550	3.314	0.720915	0.7036
10	**OTD514(1289.15-1293.7)**	Quartz monzodiorite	364	0.13111	0.512766	0.51245	5.5	585	615	6.496	0.725910	0.6922
11	**OTD514(1405.85-1410.15)**	Quartz monzodiorite	367	0.16004	0.512929	0.51254	7.4	457	423	2.988	0.718426	0.7028
12	**OTD514(2161.35)**	Quartz monzodiorite	364	0.12921	0.512773	0.51246	5.8	562	592	0.529	0.706611	0.7039
13	**OTD786(150)**	Quartz monzodiorite	376	0.13603	0.512791	0.51246	5.9	574	588	0.215	0.705068	0.7039
15	**OTD976B(266-267)**	Basalt	362	0.12359	0.512538	0.51225	1.4	892	998	0.186	0.705104	0.7041
16	**OTD976B(552)**	Basalt	362	0.14427	0.512814	0.51247	5.9	589	581	0.051	0.704155	0.7039
17	**0TB976B(772)**	Basalt dyke	362	0.14981	0.512776	0.51242	4.9	713	680	0.246	0.705530	0.7043
14	**OTD976B(1382.5-1383.5)**	Basalt	362	0.16459	0.512930	0.51254	7.2	489	441	3.910	0.723961	0.7038
18	**UUDO1A(590-593)**	Basalt	362	0.14149	0.512784	0.51245	5.4	626	628	0.084	0.704254	0.7038
19	**OTD1220(522)**	Basalt	345	0.15707	0.512801	0.51245	4.9	736	662	0.074	0.704478	0.7041
20	**OTD318(223)**	Basalt	362	0.17274	0.512830	0.51242	4.9	878	681	0.083	0.704528	0.7041

Sm, Nd, Rb and Sr contents taken from the geochemial analyses (Table 2). All ages in Ma

Tdm= one-stage (linear) DM age, essentially the same as DePaolo, Nature, 1981

Tdm*= variable crust Sm/Nd multistage after DePaolo, Linn and Schubert, JGR, 1991

Assumed parameters:

147Sm/144Nd CHUR= 0.1967; 143Nd/144Nd CHUR= 0.512638

147Sm/144Nd DM= 0.222; 143Nd/144Nd DM= 0.513114

Table 4

Click here to download Table: Table 4_fin.docx

Sample Grain/Spot	Age Ma	$^{176}Hf/^{177}Hf$	2 se	$^{176}Lu/^{177}Hf$	$^{176}Yb/^{177}Hf$	$^{176}Hf/^{177}Hf_t$	eHft	2 se	T_{DM}	T_{DM}^c
EGD001(75) Granodiorite										
#	358	0.282947	0.000028	0.001120	0.034039	0.282939	13.8	1.0	434	482
2-1	342	0.282975	0.000024	0.000962	0.026533	0.282969	14.5	0.8	392	425
2-2*	179	0.282973	0.000028	0.001950	0.062927	0.282966	10.8	1.0	406	536
3-1	348	0.282930	0.000034	0.001793	0.047955	0.282918	12.8	1.2	467	537
3-2	347	0.283004	0.000038	0.001556	0.045430	0.282994	15.5	1.3	357	365
4-1	367	0.282913	0.000022	0.001144	0.035847	0.282905	12.8	0.8	483	555
4-2	347	0.282941	0.000030	0.001384	0.039721	0.282932	13.3	1.1	446	506
5-1	343	0.283024	0.000028	0.001428	0.045250	0.283015	16.1	1.0	327	319
5-1	352	0.283006	0.000044	0.001949	0.064825	0.282993	15.6	1.5	358	363
6-1	337	0.282915	0.000024	0.000963	0.030032	0.282909	12.3	0.8	478	566
7-1	345	0.282943	0.000042	0.000720	0.022334	0.282938	13.5	1.5	435	493
8-1	351	0.282940	0.000030	0.001082	0.033313	0.282933	13.4	1.1	444	502
OTD514(1631.2-1631.7) Biotite granodiorite										
1-1	371	0.282861	0.000018	0.000907	0.02096	0.282855	11.1	0.6	553	667
2-1*	514	0.282405	0.000019	0.000756	0.02226	0.282398	-1.9	0.7	1190	1610
3-1	362	0.282922	0.000026	0.001366	0.03158	0.282913	12.9	0.9	473	541
4-1	380	0.282896	0.000040	0.002061	0.03968	0.282881	12.2	1.4	520	601
5-1	368	0.282919	0.000019	0.001929	0.04516	0.282906	12.8	0.7	484	553
6-1	371	0.282898	0.000019	0.001588	0.04391	0.282887	12.2	0.7	510	594
7-1	395	0.282915	0.000020	0.000987	0.02624	0.282908	13.5	0.7	478	531
8-1	374	0.282899	0.000020	0.001372	0.03800	0.282889	12.4	0.7	506	586
EGRDC066(172) Dacite										
1-1	372	0.282920	0.000026	0.000988	0.027727	0.282913	13.2	0.9	471	533
2-1	374	0.282904	0.000018	0.000487	0.013837	0.282901	12.8	0.6	487	561
3-1	384	0.282898	0.000032	0.001593	0.040817	0.282887	12.5	1.1	510	586
4-1	353	0.282845	0.000028	0.001810	0.050008	0.282833	9.9	1.0	590	728
5-1	363	0.282887	0.000022	0.000973	0.027289	0.282880	11.8	0.8	518	614
6-1	363	0.282867	0.000032	0.001411	0.031149	0.282857	11.0	1.1	552	666
7-1	396	0.282890	0.000030	0.000967	0.026329	0.282883	12.6	1.1	513	587
8-1	406	0.282937	0.000030	0.001060	0.027155	0.282929	14.5	1.1	448	475
9-1	366	0.282940	0.000026	0.000638	0.017412	0.282936	13.8	0.9	438	486
10-1	346	0.282905	0.000019	0.000857	0.023267	0.282899	12.1	0.7	490	581
11-1	382	0.282900	0.000022	0.001242	0.026441	0.282891	12.6	0.8	503	577
12-1	374	0.282925	0.000032	0.001528	0.041416	0.282914	13.3	1.1	471	529
OTD1218(1048-1048.8) Dacite										
1-1	344	0.282929	0.000032	0.001473	0.045817	0.282920	12.8	1.1	464	537
2-1	367	0.282983	0.000032	0.003209	0.075023	0.282961	14.8	1.1	405	427
3-1	362	0.282911	0.000028	0.001954	0.044489	0.282898	12.4	1.0	496	575
4-1	356	0.282955	0.000028	0.001645	0.050147	0.282944	13.9	1.0	429	473
5-1	354	0.282961	0.000034	0.002700	0.085581	0.282943	13.8	1.2	432	477
6-1	373	0.282925	0.000034	0.001130	0.033764	0.282917	13.3	1.2	466	524
7-1	352	0.282858	0.000034	0.002238	0.062646	0.282843	10.3	1.2	578	706
8-1	373	0.282950	0.000024	0.002148	0.065627	0.282935	14.0	0.8	442	483

OTD404(399) Dacite										
1-1	363	0.282909	0.000026	0.001963	0.044372	0.282896	12.4	0.9	499	579
2-1	360	0.282930	0.000026	0.003299	0.081775	0.282908	12.7	0.9	487	553
3-1	363	0.282888	0.000044	0.002829	0.057074	0.282869	11.4	1.5	543	640
4-1	364	0.282894	0.000032	0.002757	0.062702	0.282875	11.7	1.1	533	625
5-1	372	0.282983	0.000050	0.002993	0.065397	0.282962	14.9	1.8	403	421
6-1	356	0.283015	0.000054	0.003417	0.074112	0.282992	15.6	1.9	359	363
7-1	352	0.282988	0.000040	0.001322	0.038620	0.282979	15.1	1.4	378	395
8-1	378	0.282980	0.000036	0.002852	0.068474	0.282960	15.0	1.3	406	423
EGRCD0073 Quartz monzodiorite								0.0		
1-1	360	0.282913	0.000026	0.000953	0.029113	0.282907	12.7	0.9	480	556
2-1	324	0.282946	0.000028	0.001335	0.039506	0.282938	13.0	1.0	438	508
3-1	358	0.282964	0.000028	0.001965	0.059567	0.282951	14.2	1.0	419	456
4-1	370	0.282994	0.000032	0.001739	0.051859	0.282982	15.6	1.1	373	377
5-1	363	0.282937	0.000032	0.001534	0.045024	0.282927	13.5	1.1	453	508
6-1	352	0.282947	0.000032	0.001654	0.051622	0.282936	13.5	1.1	440	494
7-1	355	0.282978	0.000020	0.001177	0.036740	0.282970	14.8	0.7	390	414
8-1	356	0.282957	0.000024	0.001339	0.041191	0.282948	14.1	0.8	422	464
9-1	364	0.282937	0.000026	0.001161	0.035237	0.282929	13.6	0.9	449	502
OTD258(82.5) Quartz monzodiorite								0.0		
1-1	353	0.282898	0.000022	0.001232	0.03246	0.282890	11.9	0.8	505	599
2-1	352	0.282890	0.000040	0.001799	0.04676	0.282878	11.5	1.4	525	626
3-1	365	0.282887	0.000026	0.002004	0.05492	0.282873	11.6	0.9	532	629
4-1	357	0.282897	0.000026	0.001860	0.05147	0.282885	11.8	0.9	516	608
5-1	351	0.282893	0.000024	0.001020	0.02793	0.282886	11.8	0.8	510	608
6-1	362	0.282866	0.000024	0.001573	0.04569	0.282855	10.9	0.8	556	672
OTD343(1247) Quartz monzodiorite			0.000000							
1-1	360	0.282923	0.000022	0.002556	0.07513	0.282906	12.7	0.8	487	558
2-1	358	0.282962	0.000020	0.003954	0.12591	0.282936	13.7	0.7	446	491
3-1	369	0.282911	0.000022	0.001821	0.05564	0.282898	12.6	0.8	495	569
4-1	370	0.282930	0.000026	0.003684	0.10883	0.282904	12.8	0.9	492	554
5-1	348	0.282979	0.000032	0.003354	0.10021	0.282957	14.2	1.1	413	448
6-1	371	0.282983	0.000028	0.003270	0.10616	0.282960	14.8	1.0	406	426
7-1	382	0.282979	0.000022	0.002889	0.08800	0.282958	15.0	0.8	408	423
8-1	366	0.282883	0.000032	0.002368	0.06590	0.282867	11.4	1.1	543	643
OTD514(1289.15-1293.7) Quartz monzodiorite										
1-1	353	0.282929	0.000028	0.000958	0.022392	0.282923	13.1	1.0	458	524
1-2	358	0.282941	0.000018	0.001539	0.041356	0.282931	13.5	0.6	448	502
2-1	364	0.282920	0.000022	0.002083	0.058041	0.282906	12.7	0.8	485	555
3-1	368	0.282972	0.000044	0.002070	0.048401	0.282958	14.7	1.5	409	434
4-1	368	0.282922	0.000024	0.000767	0.022203	0.282917	13.2	0.8	465	528
5-1	374	0.282939	0.000024	0.000981	0.027112	0.282932	13.9	0.8	444	489
6-1	357	0.282932	0.000050	0.001799	0.036867	0.282920	13.1	1.8	464	527
OTD514(1405.85-1410.15) Quartz monzodiorite										
1-1	364	0.282999	0.000030	0.002793	0.089237	0.282980	15.4	1.1	377	386
2-1	362	0.282980	0.000040	0.001094	0.033263	0.282973	15.1	1.4	387	404
3-1	367	0.282933	0.000026	0.000682	0.021226	0.282928	13.6	0.9	449	502
4-1	367	0.282929	0.000028	0.001572	0.048052	0.282918	13.2	1.0	465	525
5-1	344	0.282967	0.000042	0.001273	0.040162	0.282959	14.2	1.5	407	447
6-1	367	0.283009	0.000030	0.001636	0.051386	0.282998	16.1	1.1	350	343
7-1	362	0.282948	0.000036	0.001699	0.053117	0.282936	13.8	1.3	439	486
8-1	351	0.282965	0.000028	0.000624	0.019083	0.282961	14.4	1.0	403	438

OTD514(2161.35) Quartz monzodiorite										
1-1C	353	0.283013	0.000050	0.001414	0.036070	0.283004	16.0	1.8	342	339
1-1R	353	0.282929	0.000028	0.001155	0.035493	0.282921	13.0	1.0	460	527
2-1	353	0.282918	0.000026	0.001005	0.030507	0.282911	12.7	0.9	474	550
3-1	352	0.282969	0.000028	0.001164	0.037105	0.282961	14.4	1.0	403	436
4-1	364	0.282942	0.000022	0.000937	0.028299	0.282936	13.8	0.8	439	487
5-1	361	0.282956	0.000034	0.001566	0.034624	0.282945	14.1	1.2	426	467
6-1	347	0.282935	0.000022	0.001611	0.053454	0.282925	13.0	0.8	457	523
OTD786(150) Quartz monzodiorite										
1-1	391	0.282939	0.000038	0.001935	0.061221	0.282925	14.0	1.3	455	494
2-1	374	0.282948	0.000032	0.001148	0.037736	0.282940	14.2	1.1	433	471
2-2	368	0.282878	0.000028	0.000924	0.029004	0.282872	11.6	1.0	530	631
3-1	367	0.282989	0.000032	0.002367	0.072977	0.282973	15.2	1.1	387	400
4-1	358	0.282951	0.000024	0.001186	0.037768	0.282943	13.9	0.8	429	474
5-1	382	0.282883	0.000028	0.000967	0.029741	0.282876	12.1	1.0	523	611
6-1	388	0.282907	0.000026	0.000545	0.016929	0.282903	13.2	0.9	484	546
7-1	364	0.282939	0.000028	0.001228	0.039090	0.282931	13.6	1.0	447	499
9-1	367	0.282931	0.000026	0.001093	0.032077	0.282923	13.4	0.9	457	513
9-2	385	0.282941	0.000032	0.001480	0.047809	0.282930	14.1	1.1	447	486
10-1	372	0.282948	0.000046	0.000838	0.027386	0.282942	14.2	1.6	429	467

$^{176}Hf/^{177}Hf_t$, εHf and T_{DM} are calculated using the $^{206}Pb/^{238}U$ age of grain; ages in Ma.

T_{DM}^{C} (crustal) is calculated using a two-stage evolution assuming a mean $^{176}Lu/^{177}Hf$ ratio of crust = 0.015.

* Data rejected as ages are anomalous

Table 5

Click here to download Table: Table 5_Pb.xls

Table 5. Pb isotopes

#	Sample Nr	Lithology	Age	U	Th	U/Pb	Th/Pb	Pb	U/Th	$^{238}U/^{204}Pb$
1	**EGD001(75)**	Granodiorite	348	3.74	7.54	0.47	0.94	8	0.50	29.9
2	**OTD514(1631.2-1631.7)**	Biotite granodiorite	374	1.51	3.67	0.19	0.46	8	0.41	11.9
3	**EGRDC066(172)**	Dacite	374	1.57	3.54	0.07	0.15	23	0.44	4.3
4	**OTD1218(1048-1048.8)**	Dacite	361	1.17	2.64	0.12	0.26	10	0.44	7.3
5	**OTD404(399)**	Dacite	362	0.68	0.84	0.09	0.11	8	0.81	5.3
6	**EGRCD073(120)**	Quartz monzodiorite	361	2	3.39	0.40	0.68	5	0.59	25.4
7	**OTRCD388(504)**	Quartz monzodiorite	364	0.64	0.75	0.01	0.01	53	0.85	0.7
8	**OTD258(82.5)**	Quartz monzodiorite	359	2.48	4.03	0.08	0.13	30	0.62	5.1
9	**OTD343(1247)**	Quartz monzodiorite	366	1.92	3.33	0.38	0.67	5	0.58	24.4
10	**OTD514(1289.15-1293.7)**	Quartz monzodiorite	364	0.32	0.67	0.00	0.01	93	0.48	0.2
11	**OTD514(1405.85-1410.15)**	Quartz monzodiorite	367	0.68	3.08	0.02	0.10	32	0.22	1.3
12	**OTD514(2161.35)**	Quartz monzodiorite	364	1.64	2.32	0.33	0.46	5	0.71	20.8
13	**OTD786(150)**	Quartz monzodiorite	376	1.37	2.79	0.11	0.23	12	0.49	7.2
15	**OTD976B(266-267)**	Basalt	362	0.99	3.81	0.20	0.76	5	0.26	12.5
16	**OTD976B(552)**	Basalt	362	0.24	1.1	0.05	0.22	5	0.22	3.0
17	**0TB976B(772)**	Basalt dyke	362	0.57	1.47	0.10	0.25	6	0.39	6.0
14	**OTD976B(1382.5-1383.5)**	Basalt	362	0.32	0.72	0.03	0.06	12	0.44	1.7
18	**UUDO1A(590-593)**	Basalt	362	0.62	2.78	0.09	0.40	7	0.22	5.6
19	**OTD1220(522)**	Basalt	345	0.49	1.17	0.10	0.23	5	0.42	6.1
20	**OTD318(223)**	Basalt	362	0.27	0.6	0.03	0.08	8	0.45	2.1

App 1_Mineralogy
Click here to download Table: Appendix 1_Mineralogy.docx

Appendix 1

Sample	Mineral composition	Alteration
EGD001(75) Granodiorite	45% plagioclase, as large tabular crystals or small crystals intergrown with Kf 25% K-feldspar, generally intergrown with plagioclase 10% hornblende 7% biotite 12% quartz. *Accessories:* zircon as large grains (0.2mm), and sphene in hornblende	Epidote and fine sericite replacing plagioclase.
OTD 514 (1631.2-1631.7) Biotite granodiorite	40% plagioclase occurs in equant crystals, or as glomeroporphyritic aggregates. 5% quartz occurs as small resorbed phenocrysts 15% ferromagnesian minerals, biotite and hornblende in about equal proportions. Groundmass comprises fine felted laths of feldspar and quartz, forming mosaic-like aggregates about 50 micron in diameter. These aggregrates may include some microgranophyric intergrowths. *Accessories: P*ossible allanite as inclusion in quartz. No zircon observed.	Ferromagnesian minerals are chlorite altered. Plagioclase is albite, sericite and calcite altered. Groundmass alteration difficult to discern, and includes, albite, quartz, sericite and calcite.
EGRCD066(172) Dacite	Presumed to be of dacitic composition, due to the presence of quartz phenocrysts. 40% plagioclase (altered to albite and sericite) 20% relict biotite and hornblende in about equal proportion Matrix is quartz-rich. *Accessories:* 20 micron-sized zircons are present in the quartz-rich matrix.	Plagioclase phenocrysts are albitized, and have fine sericite alteration. Ferromagnesian phases are altered to chlorite and iron oxides. Epidote occurs in veins, and replaces plagioclase.
OTD1218 (1048-1048.8) Dacite	Dacitic composition is inferred from the presence of small amounts of quartz crystals (5%). 40% plagioclase crystals 10% andesitic to dacitic rock fragments 42% quartz-feldspar-rich groundmass highly altered 3% biotite altered to sericite and quartz. *Accessories:* zircon, monazite(?), rutile and apatite are found.	All ferromagnesian minerals are completely altered to sericite and opaque minerals. Plagioclase is albite and sericite altered. The groundmass is strongly quartz-sericite altered.
OTD404(399) Dacite	45% plagioclase as phenocrysts >2.5mm 5% quartz phenocrysts 5% ferromagnesian minerals (possibly biotite), completed altered 45% recrystallized quartz-feldspar-rich matrix *Accessories:* apatite is common as fine needles, and monazite is present as large corroded grains.	Original ferromagnesian minerals altered to sericite, chlorite and opaque minerals. All plagioclase is affected by fine sericitic alteration, and brown hematite dusting, imparting a red color in hand specimen.

EGRCD073(120) Quartz monzodiorite	70% feldspar, with K-feldspar to plagioclase about 2: 3. Plagioclase is early and commonly intergrown with later K-feldspar. 10% quartz, interstitial between feldspar crystals 20% ferromagnesian minerals, now represented by mainly chlorite and epidote.	All ferromagnesian minerals are altered to actinolite, chlorite, epidote, quartz, sphene and opaques.
OTRCD388(504) Quartz monzodiorite	Complete recrystallization to fine-grained quartz and muscovite.	Small patches of chlorite apparently replace fine muscovite alteration. Dark opaques are fine-grained bornite.
OTD258(82.5) Quartz monzodiorite	55% muscovite (sericite) replacing original plagioclase phenocrysts and matrix 34% quartz, mainly in granular aggregates (0.1mm) replacing original matrix 10% pyrite 1% topaz, rutile, and tourmaline.	Rutile appears to mark former ferromagnesian mineral sites as very fine grains, whereas tourmaline and topaz occurs with muscovite alteration. The topaz forms relatively large zoned grains, up to 20 microns. Inclusions that outline the zones are possibly rutile. Plagioclase phenocrysts are entirely replaced by fine muscovite, whilst ferromagnesian minerals appear to be replaced by quartz in oriented mosaic-like patches (see image above), together with fine rutile. No zircon was observed in the thin section.
OTD343(1247) Quartz monzodiorite	Highly recrystallized porphyritic texture, very faint ghosts of phenocrysts are visible in hand specimen, but in thin section the rock comprises patches of quartz and sericite.	Intense quartz sericite alteration. Some resistate minerals (possibly monazite) are present but appear to be corroded by the intense sericite alteration. No zircons were observed.
OTD514 (1289.15-1293.7) Quartz monzodiorite	Now composed of about 50% quartz and 45% muscovite; the remainder – mainly sulfides, and accessory minerals. *Accessories:* pale brown translucent prisms of possible zircon (?), with darker red granules of rutile. Rutile also occurs as inclusions in this mineral.	
OTD514 (1405.85-1410.15) Quartz monzodiorite	Due to alteration the sample comprises approximately 45% quartz and 50% muscovite. The remainder includes bornite and chalcopyrite. *Accessories:* <1% accessory monazite, apatite and zircon.	
OTD514(2161.35) Quartz monzodiorite	60% plagioclase 10% quartz, partly secondary 10% K-feldspar alteration intergrown with quartz 20% completely altered ferromagnesian minerals (chlorite, opaques).	Pink K-feldspar intergrown quartz veins, and forming selvages to quartz veins. Very fine clay hematite dusting affects all feldspar minerals and imparts a red color in hand specimen. In addition, fine sericite replaces feldspar. All primary ferromagnesian phases are completely altered to chlorite, sericite and opaques.
OTD786(150) Quartz monzodiorite	70% plagioclase 20% chlorite and calcite, in patches up to 3mm, which represent sites of former ferromagnesian minerals. 5% quartz in fine-grained aggregates filling interstitial sites (above) 3% opaques. *Accessories:* apatite, 1 zircon was observed.	Complete destruction of ferromagnesian phases, to chlorite and calcite, opaques. Apatite occurs in original ferromagnesian sites. Plagioclase is relatively unaltered, but exhibits a fine hematite dusting, giving the red appearance in hand specimen. Interstitial infillings could be more sodic plagioclase (albite) + quartz.

OTD976B (266-267) Basalt	40% augite as phenocrysts >1mm 35% plagioclase in groundmass 15% ferromagnesian minerals in groundmass (now completely altered to chlorite) 10% unidentified patches of quartz-epidote alteration, may represent original glass.	Original augite crystals appear to be serpentized, as well as chlorite altered. Chlorite is also very widespread in the groundmass, and the rock may now comprise up to 25% chlorite. Plagioclase crystals are albitized and albite in-fills vesicles (see above). 3% epidote with 7%quartz as irregular patches, possibly after volcanic glass.
OTD976B(552) Basalt	45% augite, with 35% as phenocrysts >0.2mm 25% plagioclase phenocrysts 30% fine-grained matrix, dominated by tiny laths of plagioclase, altered ferromagnesian minerals and fine opaques. Minerals indicating quartz undersaturation, such as olivine and feldpathoids apparently are absent.	Actinolite-chlorite lines dissolution vugs are found in the fine-grained matrix. Plagioclase is partly albitized and sericite altered.
OTD976B(772) Basalt dyke	45% augite (35% as phenocrysts and 10% in groundmass) 40% plagioclase 10% unidentified ferromagnesian phenocryst, altered to chlorite 3% opaque minerals, 2% accessory minerals, mainly apatite.	15% chlorite, replacing unidentified phenocryst (above) and in groundmass. Albite replaces plagioclase and occurs in patches replacing the groundmass. 5% calcite in the groundmass and as veins.
OTD976B (1382.5-1383.5) Basalt	35% former augite phenocrysts altered to quartz-sericite 60% secondary biotite altered to chlorite, calcite and sericite 5% sulfides.	Original basalt composition, but now extensively altered. The most conspicuous alteration is secondary biotite in aggregates 20-50microns, partly altered to chlorite. Interstitial patches to biotite are calcite and sericite.
UUDO1A(590-593) Basalt	10% unidentified ferromagnesian phenocrysts (possibly hornblende?), altered to chlorite, Fe-oxides, and quartz 10% fine granular magnetite 70% acicular plagioclase 10% calcite, 1% epidote.	Plagioclase is albitized, all primary ferromagnesian minerals are altered to chlorite or epidote, chlorite and calcite replaces the groundmass.
OTD1220(552) Basalt	65% plagioclase, 20% chlorite, replacing matrix, former unidentified ferromagnesian phases, and in rare cases also plagioclase phenocrysts. 5% calcite in orbicular structures with fine dark unidentified opaques 3% granular magnetite.	Strong chlorite-calcite alteration, complete destruction of all primary ferromagnesian phases.
OTD318(223) Basalt	Due to alteration the only primary phases that are identified are: 40% augite (phenocrysts) 30% plagioclase 2% magnetite. *Accessories:* zircon as large grains (0.2mm), and sphene in hornblende.	Large augite phenocrysts are relatively unaltered, but smaller crystals (1mm) are partly altered to chlorite. Albite occurs in small patches (<0.5mm), usually together with epidote or chlorite. Alteration minerals comprise about 20% of the sample; 7% epidote, 10% chlorite, 3% albite.